# Supplementary Information

## Sustainable Existence of Solid Mercury (Hg) Nanoparticles at Room Temperature and Their Applications

Villa Krishna Harika†,[a], Tirupathi Rao Penki†,[a], Boddapati Loukya[b], Atanu Samanta[a], Gui-Liang Xu[c], Cheng-Jun Sun[c], Ilya Grinberg[a], Francis Leonard Deepak[b], Khalil Amine[c], Doron Aurbach*,[a] and Aharon Gedanken*,[a]

[a]Bar-Ilan Institute for Nanotechnology and Advanced Materials (BINA) and Department of Chemistry, Bar-Ilan University, Ramat-Gan, 5290002, Israel.

[b]Nanostructured Materials Group, Department of Advanced Electron Microscopy Imaging and Spectroscopy, International Iberian Nanotechnology Laboratory (INL), Avenida Mestre Jose Veiga, Braga, 4715-330, Portugal.

[c]Chemical Sciences and Engineering Division, Argonne National Laboratory, 9700 South Cass Avenue, Lemont, IL, 60439, USA.

† Equal contribution
*E-mail: Aharon.Gedanken@biu.ac.il and Doron.Aurbach@biu.ac.il

### Abstract

Although liquid mercury (Hg) has been known since antiquity, the formation of stable solid nano forms of Hg at room temperature has not been reported so far. Here, for the first time, we report a simple sonochemical route to obtain solid mercury nanoparticles, stabilized by reduced graphene oxide (RGO) at ambient conditions. The as-formed solid Hg nanoparticles were found to exhibit remarkable rhombohedral morphology and crystallinity at room temperature. Extensive characterization using various physiochemical techniques revealed the unique properties of the solid nanoparticles of Hg compared to its bulk liquid metal phase. Furthermore, the solid nature of the Hg nanoparticles was studied electrochemically, revealing distinctive properties. We believe that solid Hg nanoparticles have the potential for important applications in the fields of electroanalytical chemistry and electrocatalysis.

## Table of content

Page No

### *Synthesis of Reduced Graphene Oxide:*

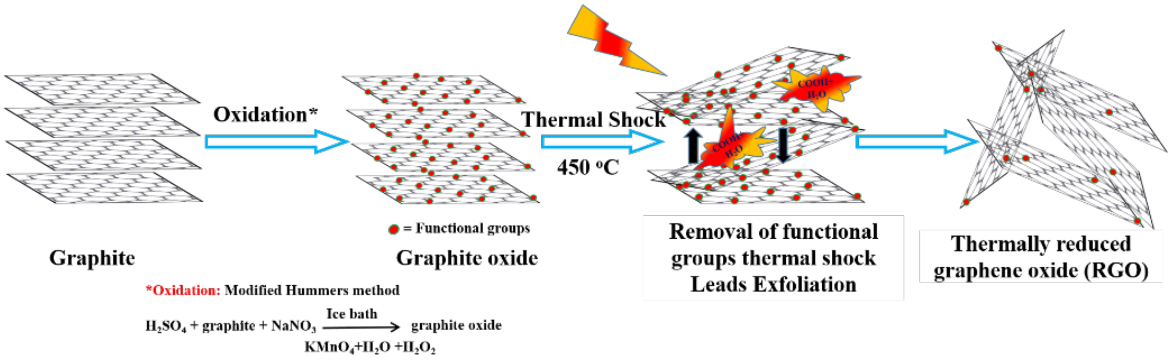

Scheme S1. Synthesis of graphite oxide through Hummers method followed by the synthesis of reduced graphene oxide by low temperature thermal shock leading to exfoliation.

***Electrochemical studies:***

(a)

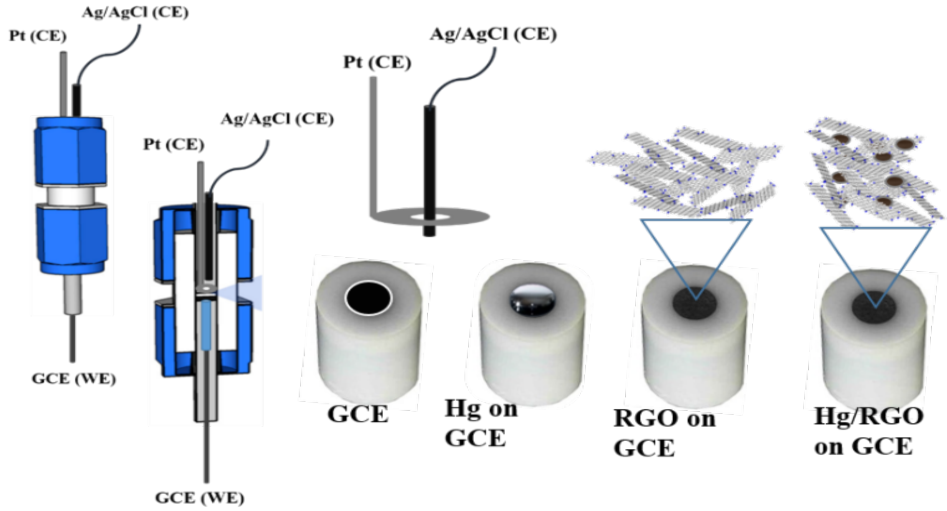

(b)

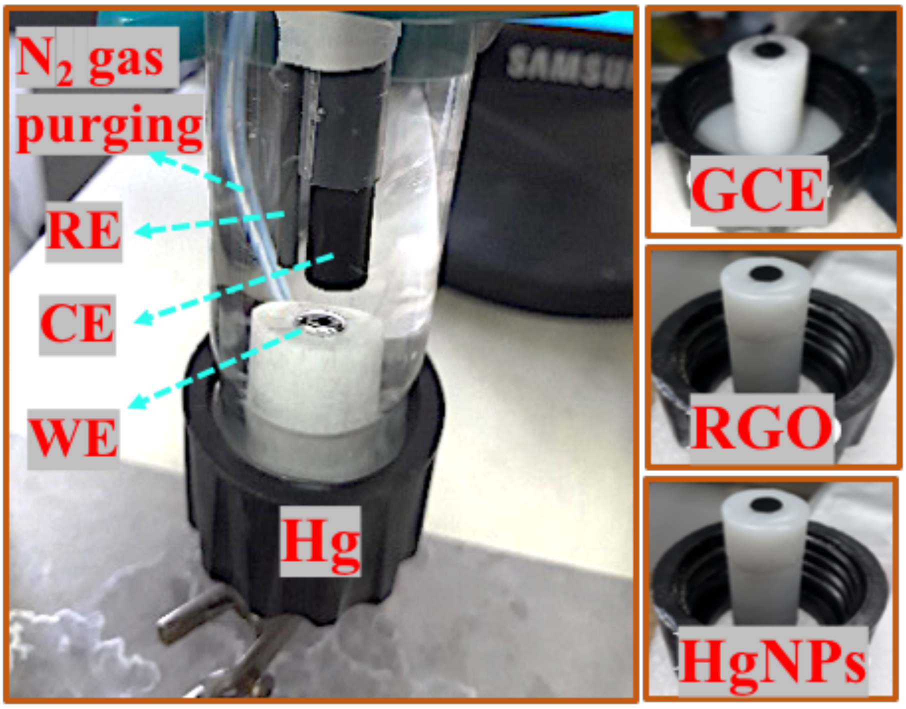

Scheme S2. Schematic description of the three electrodes cells used here. (a) - Typical cells in Swagelok setups have used for the cyclic voltammetric measurements of Fe(II)/Fe(III) and Zn/$Zn^{+2}$ solutions and (b) - Conventional electrochemical cells were used for measuring the electro-catalytic activity of hydrogen evolution reaction in 0.5 M $H_2SO_4$.

**Reference experiments.**

Several reference sonication experiments with mercury in aqueous and non-aqueous media were carried out as described below.

Pure mercury, a liquid at room temperature (melting point of -38.6 $^{o}$C), forms in water or in organic liquids two immiscible phases at room temperature. Inducing ultrasonic energy to such systems, through the solvents, results in the dispersion of liquid Hg metal into microscopic spheres because of the cavitation phenomena as presented in Scheme S3 and Videos S1-S3. The stability of the resultant product formed through this process varies depending on the solvents used for dispersion. Sonication of liquid Hg in aqueous media (0.5 grams of Hg in 20 ml of water during 6 hours) results in the dispersion of the liquid metal into small spheres but once the irradiation is ceased the dispersed spheres re-coalesce and returns to the original state (a bulk liquid Hg phase) leaving the solvent clear (scheme S3a and Video S1). It was clear that this operation (which included capable cavitation phenomena) did not form any Hg oxide phase, what enabled a smooth coalescence of the Hg micro-drops formed by sonication back to a bulk liquid mercury phase. It is also well known that the mercury carbide is an unstable moiety.

Hg microspheres in organic liquids (dodecane) were prepared in a similar manner (0.5 grams of Hg in 20 ml of solvent, sonication during 6 hours), scheme S3b and Video S2. At the end of 6 hours sonication a grey powder precipitate was obtained. The precipitate was separated by centrifugation at 8000 rpm, washed thoroughly with acetone and dried under vacuum. This process produced Hg spheres coated by carbon, as was analyzed by several characterization techniques. The size of the Hg spheres varied from 10 to 50 µm size (ESEM). EDAX analysis confirmed the presence the of C and Hg elements along with a small weight percent of O which might originate from atmospheric oxygen (Figure S1). In fact, the Hg spheres formation in organic liquids (no further coalescence) is due to coating by a carbon film around the Hg liquid spheres. A similar phenomenon was observed with Ga microspheres in our previous studies [1].

Scheme S3c and Video S3 presents for comparison the result of sonicating Hg in an aqueous medium containing RGO sheets. This process and its products which are the focus of the work reported herein, are discussed thoroughly herein. The carbon coated Hg microspheres thus obtained were characterized by DSC as shown in Figure S2. In the first heating/cooling cycle (the black thermogram) of the Hg microspheres, upon their heating from -50 to 200 $^{o}$C an endothermic peak appeared at -38.6 $^{o}$C which is due to the melting temperature of solid Hg. Cooling back from 200 to -50 $^{o}$C showed an exothermic process around -41 $^{o}$C which reflects solidification of the liquid Hg spheres coated with carbon. In the second cycle thermogram (red line) the solid Hg spheres reheated back exhibited a similar endothermic peak for melting around -38.6 $^{o}$C. All of these measurements confirmed that sonication of Hg in an aqueous medium just disperses the liquid mercury into droplets, while Hg sonication in an organic medium forms micrometric droplet encapsulated in carbon shells. These reference experiments emphasize the uniqueness of the synthetic process that forms solid state Hg nanoparticles, and reveals completely different DSC results as described and discussed herein.

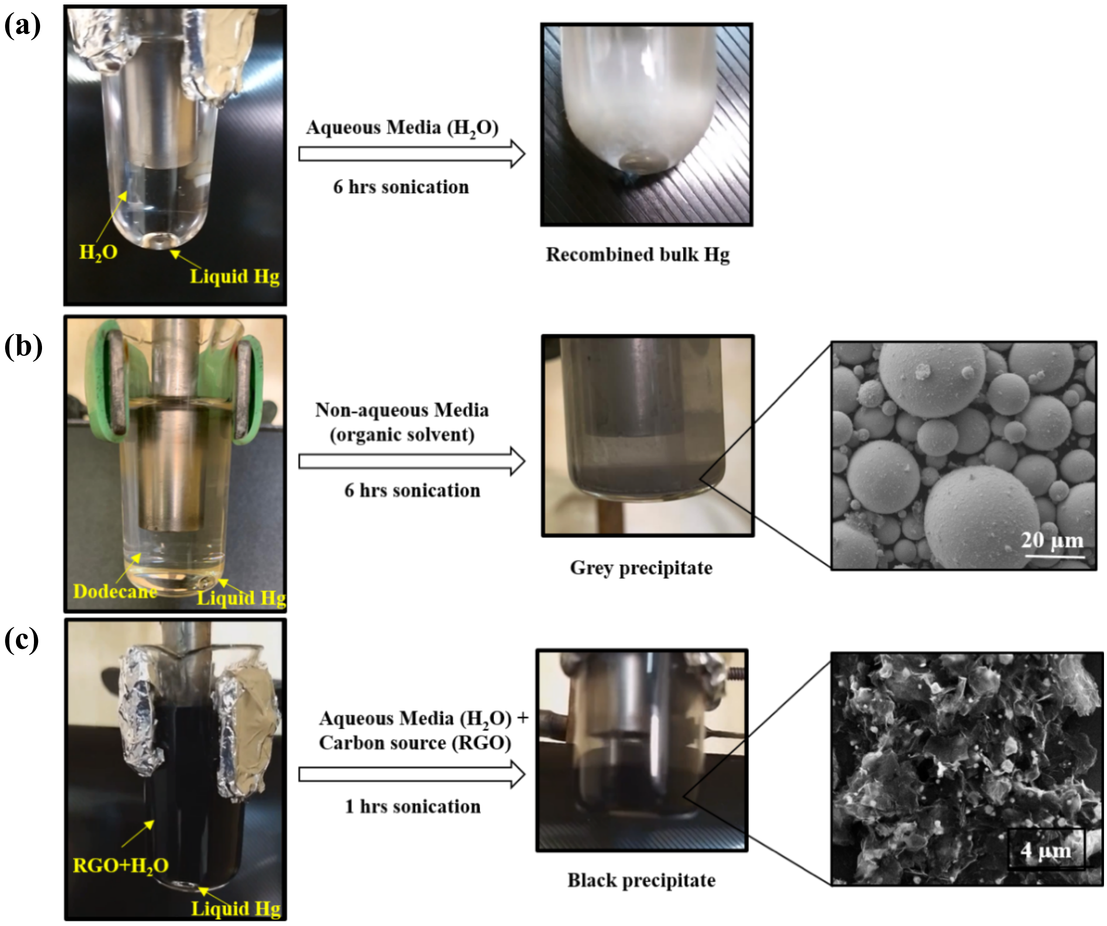

Scheme S3. Photographic representation of sonication process of Hg in (a) water, (b) organic solvent (dodecane) and (c) RGO aqueous dispersion.

## *In-situ carbon coating around microspheres:*

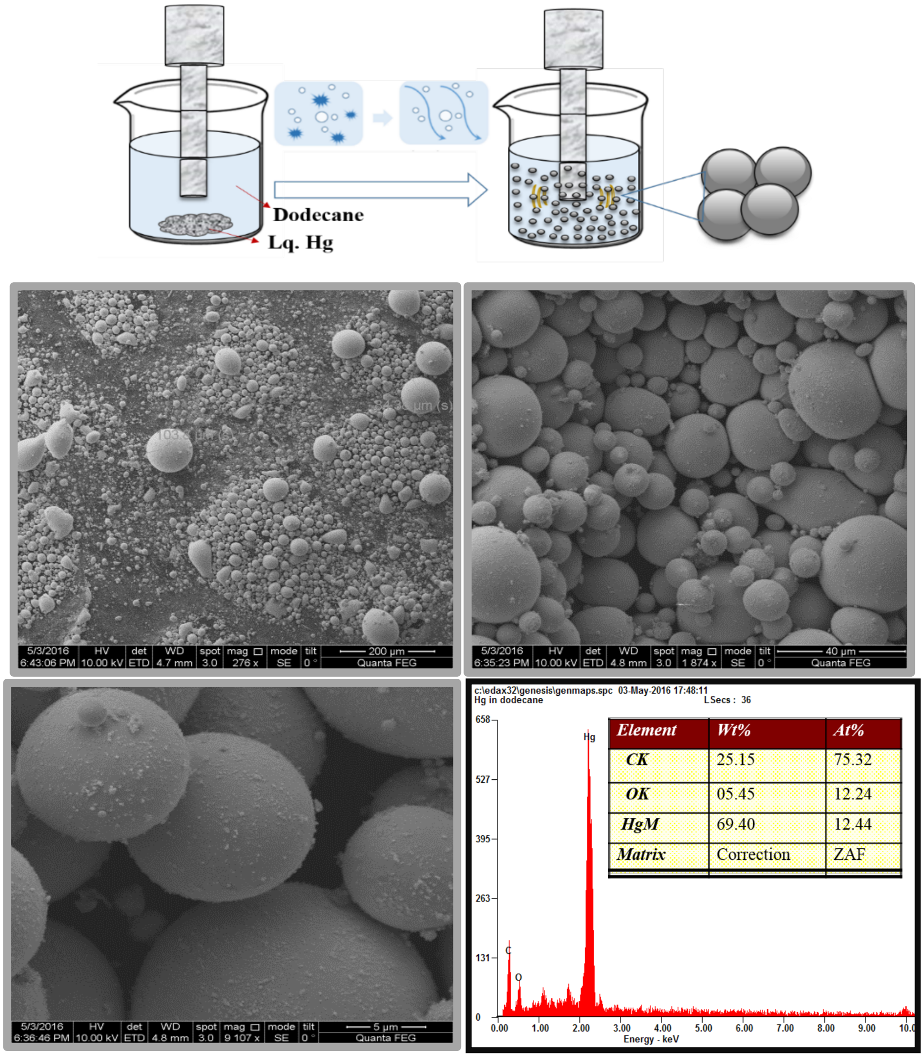

| *Element* | *Wt%* | *At%* |
|---|---|---|
| ***CK*** | 25.15 | 75.32 |
| ***OK*** | 05.45 | 12.24 |
| ***HgM*** | 69.40 | 12.44 |
| ***Matrix*** | Correction | ZAF |

Figure S1. Synthesis schematic, ESEM at different magnifications and EDAX of Hg microsphere synthesized sonochemically in an organic solvent.

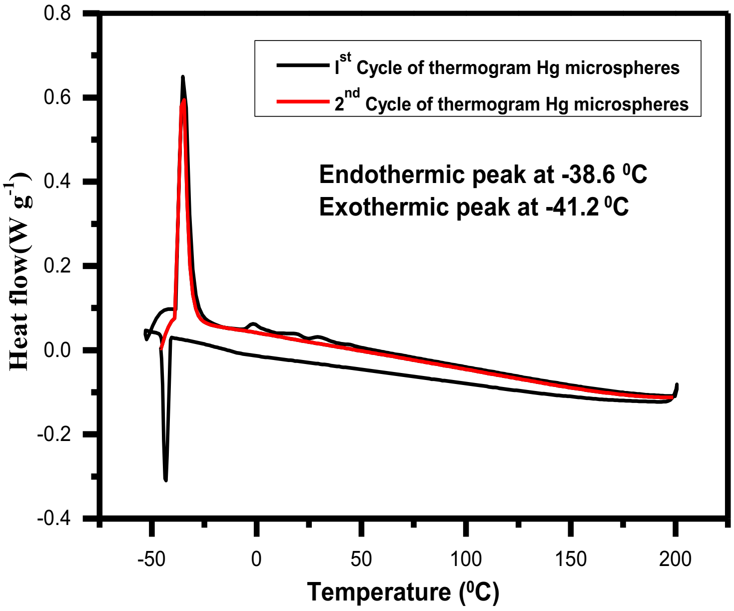

Figure S2. DSC thermograms with heat and freeze cycles of Hg microspheres synthesized in organic solvent at a rate of 5 k/ min

**ICP-AES analysis :**

It was important to reject the possibility that the sonication process forms amalgams of mercury with traces of sodium and potassium that may present as ions in the mixtures used for the synthesis. Such amalgams if formed, could play an important role in the stabilization of a new mercury phase.

Elemental analysis of the synthesized HgNPs were carried out using the ICP technique (ICP–AES, spectrometer Ultima-2 from Jobin Yvon Horiba) (Figure S3 (i)). For the ICP analysis HgNPs samples were prepared in two batches. For a sample preparation ~ 10 mg of sample powder of HgNPs was weighed and then dissolved in 1 ml of aqua regia (1:3 of $HNO_3$:HCl) in beakers at 30 $^oC$ for about 2 h and then 9 ml of DD water were added to make up the volume to 10 ml. The undissolved RGO was filtrated using Whatman filter paper to obtain a clear solution, which was further subjected to ICP-AES. The results are tabulated below, where, the major element Hg (more than 99 %) is detected at all the dilutions of the sample preparation as follows. In the analysis, K and Na are detected at very low percentage, and the blank containing DD water and aqua regia also contribute to a very minor Na and K content. Thus, the RGO-HgNPs samples contain <0.5% of both Na and K. This indicates that there is no role of Na or K in solidifying mercury by the formation of amalgam. On top of this, even if such amalgams could be formed by a sonication process in the presence of Na or K ions, they are moisture sensitive [2–4], and cannot survive in our synthetic condition using an aqueous media.

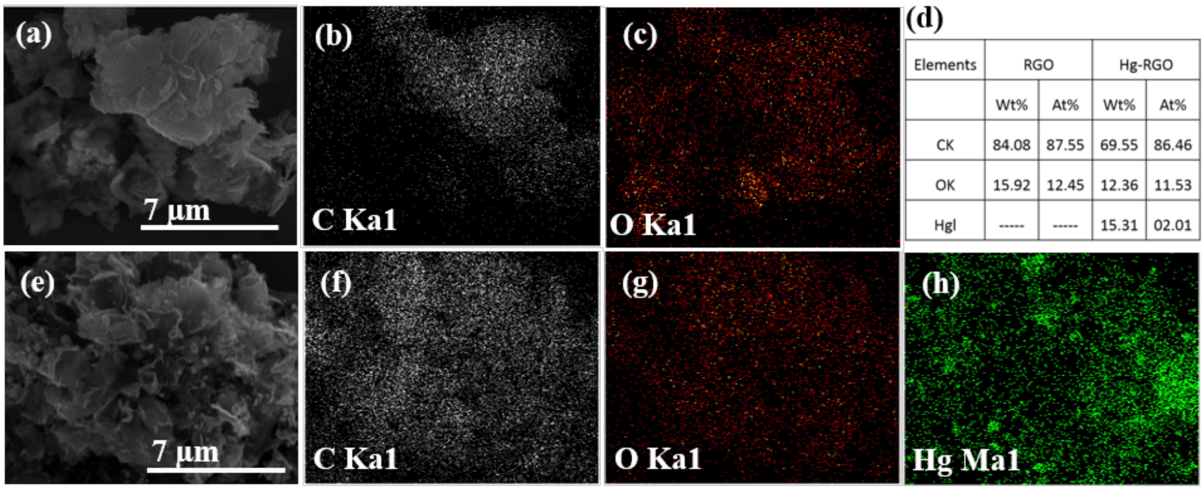

| Elements | RGO | | Hg-RGO | |
|---|---|---|---|---|
| | Wt% | At% | Wt% | At% |
| CK | 84.08 | 87.55 | 69.55 | 86.46 |
| OK | 15.92 | 12.45 | 12.36 | 11.53 |
| HgI | ----- | ----- | 15.31 | 02.01 |

**(i)**

| Elements | | Original data obtained | | | | | Percentage of Elements (*Excluding K and Na from Aqua regia) | | |
|---|---|---|---|---|---|---|---|---|---|
| | | Hg | | K | Na | | | | |
| Sample Name | | Hg 184.950 | Hg 194.227 | K 766.491 | Na 588.995 | Na 589.592 | Hg | K | Na |
| DD water | | < -0.124<br>(0.00124) | < -0.126<br>(0.00156) | < 0.026<br>(0.04227) | < -0.063<br>(0.01679) | < -0.050<br>(0.003681) | | | |
| Aqua regia (100 time dilution) | | < -0.182<br>(0.01025) | < -0.183<br>(0.01054) | < 0.069<br>(0.01043) | 0.338<br>(0.02787) | 0.318<br>(0.00544) | | | |
| HgNPs batch 1 | 10 times dilution | > 630.525<br>(7.46700) | > 666.595<br>(1.11900) | 1.858<br>(0.03076) | 5.261<br>(0.05105) | 5.249<br>(0.04699) | 99.33 | 0.23 | 0.44 |
| | 100 times dilution | ➢ 71.313<br>(0.40409) | ➢ 70.114<br>(0.56974) | 0.186<br>(0.02174) | 0.543<br>(0.03131) | 0.520<br>(0.003274) | 99.35 | 0.23 | 0.41 |
| | 1000 times dilution | 8.348<br>(0.04840) | 8.197<br>(0.10689) | < 0.025<br>(0.01429) | < 0.042<br>(0.02570) | 0.043<br>(0.00268) | 99.67 | 0.21 | 0.12 |
| HgNPs batch 2 | 10 times dilution | > 704.968<br>(8.40600) | > 741.817<br>(9.48900) | 2.332<br>(0.04028) | 6.515<br>(0.02618) | 6.49<br>(0.06923) | 99.52 | 0.18 | 0.30 |
| | 100 times dilution | ➢ 81.039<br>(0.93190) | > 79.711<br>(1.14100) | 0.259<br>(0.00170) | 0.659<br>(0.00749) | 0.665<br>(0.00512) | 99.55 | 0.16 | 0.29 |
| | 1000 times dilution | 7.259<br>(0.00598) | 7.110<br>(0.03882) | < 0.004<br>(0.01770) | < 0.006<br>(0.01449) | 0.021<br>(0.00096) | 99.76 | 0.06 | 0.18 |

Figure S3. HRSEM and elemental mapping of (a)-(c) RGO, (e)-(h) elemental composition of RGO together with HgNPs and (i) results of ICP elemental analysis of HgNPs samples (prepared from two different batches).

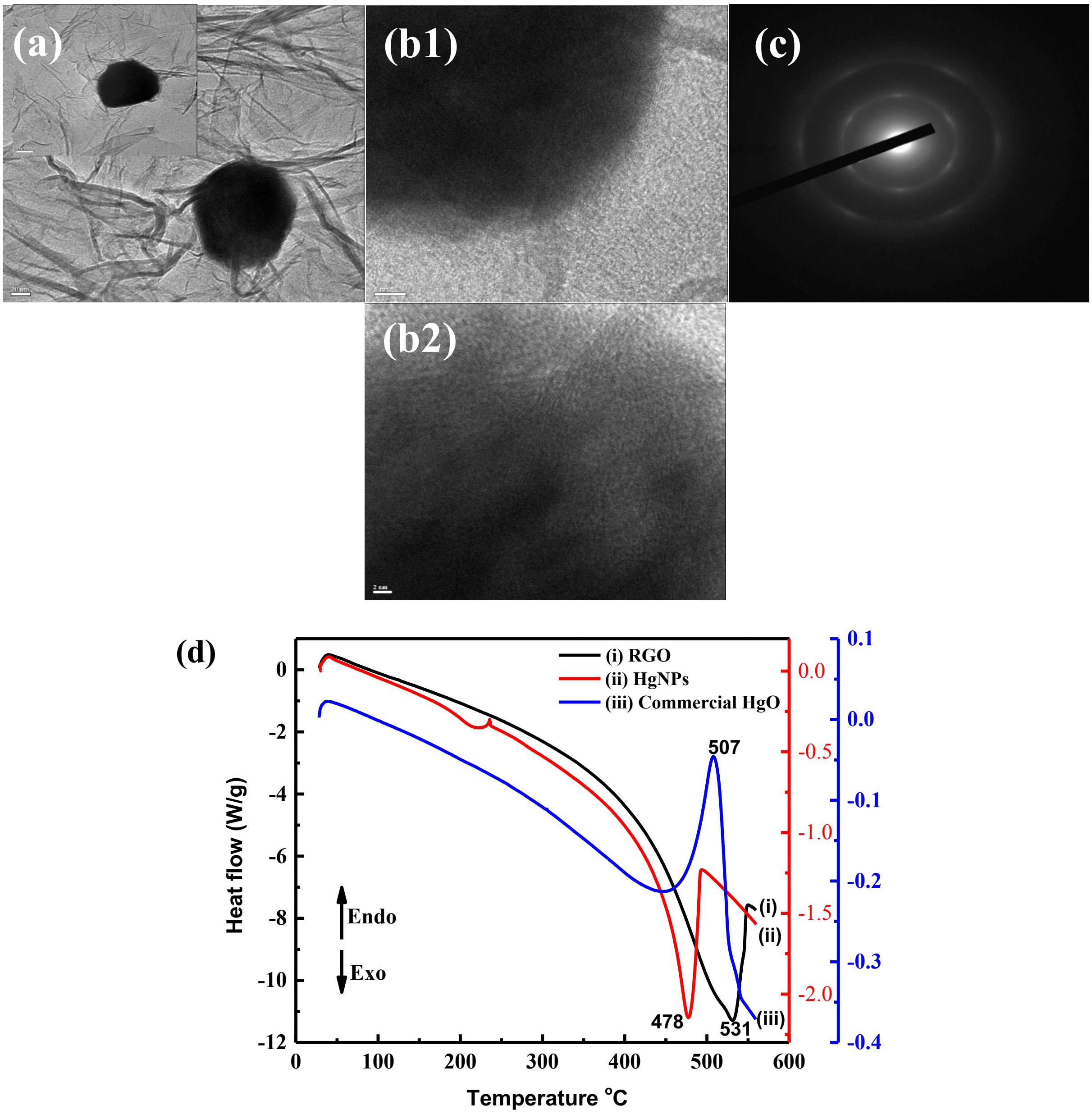

Figure S4. (a), (b1) and (b2) HRTEM images at different magnifications and (c) SAED pattern of solid HgNPs. (d) DSC thermograms of RGO (i), HgNPs (ii) and commercial HgO heated to 580 ºC

## DSC analysis:

In order to reject the possible formation of HgO in the sonication processes that were carried out, DSC measurements were carried out in which the thermal behavior of RGO, HgNPs and commercial HgO were compared (see thermograms in Figure S4). The DSC thermogram of HgO reveals an endothermic peak at 507 $^{o}$C corresponding to the melting of HgO particles which is not observed in thermograms related to HgNPs [2]. Instead we observed for the HgNPs an exothermic peak around 478 $^{o}$C which originates from the RGO component. This clearly proves that the HgNPs are not mercury oxide.

## *STEM analysis:*

There is a clear evidence for the formation of solid Hg particles entrapped within the RGO from the AC-HAADF-STEM Z-contrast imaging performed at 80 kV as shown in Figure S5 (a), S5(b) and S5(c). Though the Hg particles are not stable at this electron beam energy, imaging is performed before the Hg metal undergoes melting due to interactions with the electron beam. STEM elemental mapping detected the presence of Hg trapped in RGO as shown in Figure S5 (d) and S5 (e) Hg signal is detected in the regions of the Hg clusters on RGO, similar to those shown in Figure S5 (c).

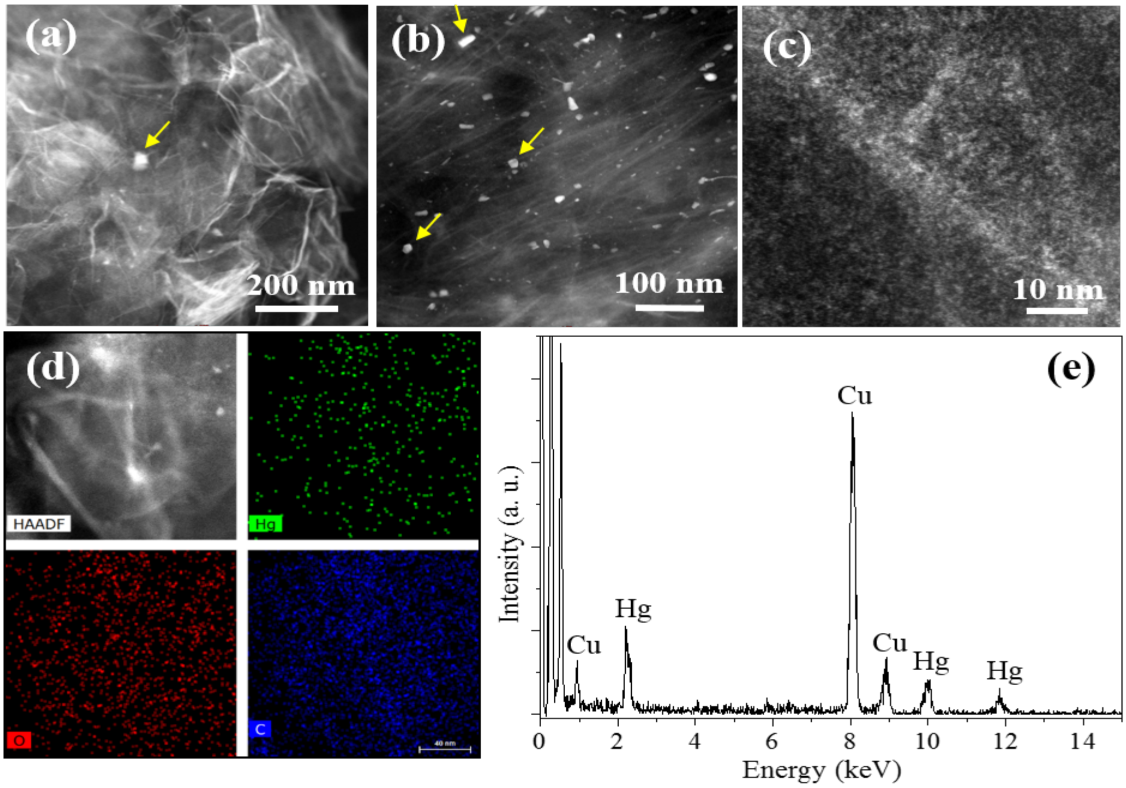

Figure S5. HAADF-STEM imaging and EDX elemental maps showing the Hg clusters. (a) and (b) indicate the presence of Hg clusters on RGO as indicated by arrows. (c) shows the Z-contrast obtained from an area of ~80 nm from the RGO sheet. (d) STEM-EDX elemental mapping of Hg, O and C. (e) Line-profile by EDX chemical mapping clearly shows the presence of Hg.

### ***HRTEM, EELS analysis:***

The high-resolution TEM imaging performed at 60 kV using gun monochromated beam is shown in Figure S6 (b) and S6 (c) while Figure S6 (a) shows the low-magnification TEM imaging performed at 200 kV in a JEOL 2100 microscope. The inset in Figure S6 (b) shows the Fourier-filtered transformed (FFT) electron diffraction from RGO imaged at high magnification. The (100) and (002) planes of RGO are resolved and the corresponding d-spacing distances are 3.56 Å and 2.08 Å respectively. Figure S6 (c) clearly shows the presence of Hg clusters trapped in RGO sheets as indicated by the arrow. In order to confirm the presence of Hg trapped in RGO, electron energy-loss spectra (EELS) were obtained from the RGO sheets. Hg $O_{2,3}$ edge was easily detected at 50 eV as shown in Figure S6 (d). The $O_{2,3}$ spectrum was extracted after a background removal using a power-law model and smoothed by Savitzky-Golay smoothing filter. In summary, by carrying out AC-TEM/STEM analysis in combination with EDAX and EELS measurements, it was possible to conclude that a pure Hg phase is present in the nanoparticles described above, without the formation of secondary phases and or/impurities.

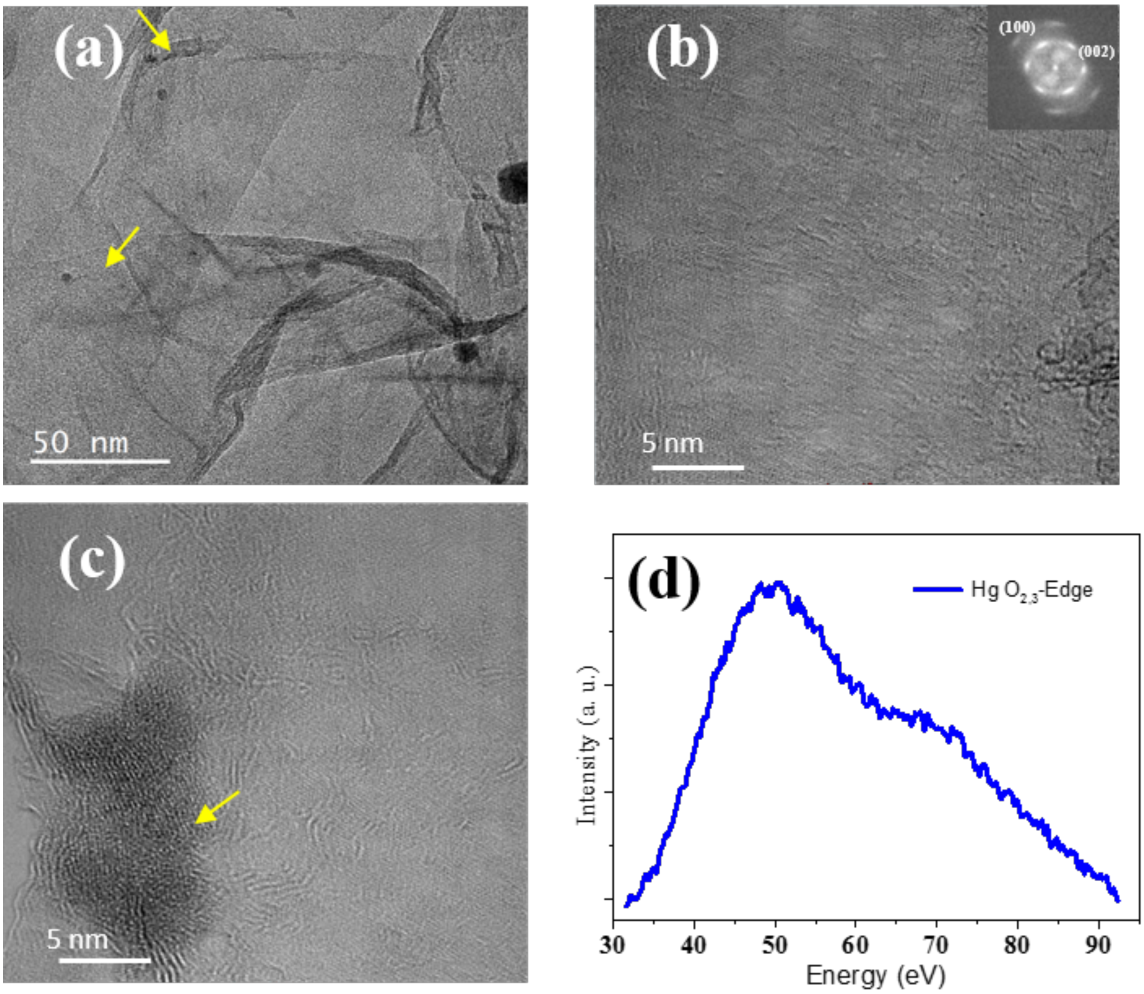

Figure S6. TEM imaging and spectroscopy (a) overview of the RGO with Hg clusters as shown by arrows, (b) RGO nanosheet along with the Fourier-filtered transform of the image in the inset, (c) showing Hg within RGO sheet at high-magnification and (d) EELS spectra of Hg $O_{2,3}$ edge.

## Effect of temperature on solid nature of the HgNPS:

In order to fully understand the DSC measurements performed to confirm the solid nature of the HgNPs, samples of the material were heated at different temperatures between 27 °C and 350 °C. The heated samples were analyzed using ESEM supported by elemental mapping and XRD patterns (Figure 3 and Figure S7). Figure S7 (a1 – a6) show ESEM, elemental mapping and EDAX spectra of the HgNPs at room temperature. Figure S7 (b1 – b6) show the microscopic imaging of HgNPs heated to 150 °C, revealing the formation of a few nanosphere droplets of Hg within RGO, along with stable HgNPs which indicates the initiation of melting of the HgNPs. On heating the samples to 250 °C, bigger micro-spherical droplets of Hg are observed as a result of the melting of the solid Hg nanoparticles which then coalesce. At that temperature, the Hg moieties escape from the graphene layers as shown in Figure S7 (c1 – c6). On further heating to 350 °C (Figure S7 (d1 – d6)), we observe the disappearance of the Hg microspheres, indicating their evaporation, since this temperature is close to the boiling point of metallic mercury.

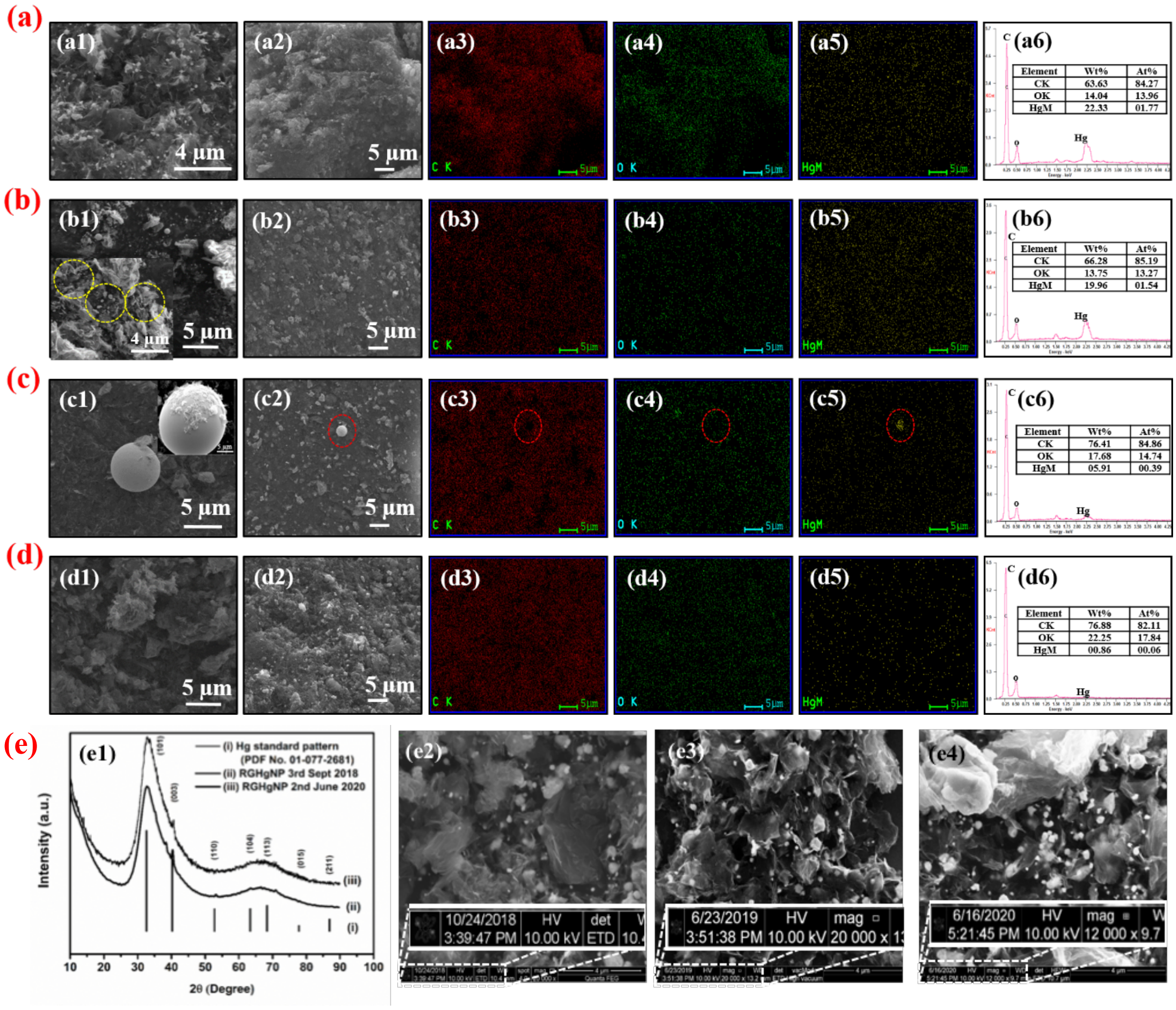

(a6)

| Element | Wt% | At% |
|---|---|---|
| CK | 63.63 | 84.27 |
| OK | 14.04 | 13.96 |
| HgM | 22.33 | 01.77 |

(b6)

| Element | Wt% | At% |
|---|---|---|
| CK | 66.28 | 85.19 |
| OK | 13.75 | 13.27 |
| HgM | 19.96 | 01.54 |

(c6)

| Element | Wt% | At% |
|---|---|---|
| CK | 76.41 | 84.86 |
| OK | 17.68 | 14.74 |
| HgM | 05.91 | 00.39 |

(d6)

| Element | Wt% | At% |
|---|---|---|
| CK | 76.88 | 82.11 |
| OK | 22.25 | 17.84 |
| HgM | 00.86 | 00.06 |

Figure S7. Displays the ESEM images, elemental mapping, EDAX and composition of (a) as-synthesized HgNPs encapsulated in RGO, HgNPs heated at (b) 150 °C, (c) 250 °C and (d) 350 °C. (e) XRD and ESEM images of HgNPs samples stored (nearly one and a half year time) at ambient condtion in the laboratory.

### ***XANES analysis:***

The chemical state of HgNPs and the bonding interaction between HgNPs and RGO was investigated using synchrotron-based X-ray absorption near-edge structure (XANES) spectroscopy. Figure 3 (a) and 3 (b) depicts the Hg $L_{III}$-edge XANES spectra and their first-derivatives for the HgNPs and for other mercury compounds (liquid Hg, $Hg_2Cl_2$, $HgCl_2$, $Hg(OOCCH_3)_2$ ,($Hg(AC)_2$, HgO) as references. In general, the X-ray absorption curves reveal two inflection points near the zero-point energy (E = 12284.0 eV) of the mercury absorption edge. These spectra show two distinct peaks in their first derivative curves and the separation between them is defined the inflection point difference (IPD) [5–7]. The IPD values and the peak height ratio have been used as a fingerprint information for the chemical identification of the various species thus measured. Figure 3 (a) and 3 (b) and Table S1 show that the HgNPs samples (8.2 eV) have low IPD values when compared to the reference oxygen-containing mercury compounds (i.e. HgO (13.3 eV), $Hg(OOCCH_3)_2$ (10.8 eV)) and mercury halides (i.e. $Hg_2Cl_2$ (8.9 eV), $HgCl_2$ (9.1 eV)). These results are in well agreement with reported literature values [5–7]. This confirms the existence of elemental mercury in the HgNPs samples rather than its oxidized forms (HgO, $Hg_2Cl_2$, $HgCl_2$, $Hg(AC)_2$. The edge is slightly shifted and the white line intensity is higher for the HgNPs samples, what clearly reflects interactions between Hg metal and graphene [8,9]. These results indicate that the HgNPs are stabilized by their contact with the RGO sheets. This stabilization results from a partial oxidation of Hg due to charge transfer between RGO and Hg. These measurements provide clear evidence for electronic interactions, which involve a slight charge transfer from the mercury (donor) to the graphene (acceptor). Such charge transfer interactions are facilitated and promoted by the fact that the graphene sheets contain oxygenated functional groups (e.g. epoxy, hydroxyl).

Table S1. Hg LIII-edge first inflection points (E1), second inflection points (E2), and inflexion points difference (IPD) in the first derivative curves of XANES spectra for SSHgNPs and reference mercury compounds.

| **Materials** | **E1 (eV)** | **E2 (eV)** | **peak separation (IPD)=E2-E1 (eV)** |
|---|---|---|---|
| Liq Hg | 12284.0 | ------ | ------- |
| SSHgNPs | 12285.7 | 12293.9 | 8.2 |
| $Hg_2Cl_2$ | 12283.3 | 12292.2 | 8.9 |
| $HgCl_2$ | 12283.8 | 12292.9 | 9.1 |
| $Hg(OOCCH_3)_2$ | 12283.6 | 12294.4 | 10.8 |
| HgO | 12282.1 | 12295.4 | 13.3 |

***Theoretical analysis:***

Models that seem to represent very well possible interactions between Hg particles and graphene/RGO sheets (both) were elaborated. Hg particles comprised of 32 or 122 mercury atoms and graphene sheets containing 122 or 240 carbon atoms were utilized, as illustrated in Figures S8 (a) – S8 (f). Such structures can be used as reasonable models for simulating the experimental findings reported herein, which present also the effect of sizes.

The total energy change was calculated from ab-initio density functional theory using the formula $\Delta E = E_{(Hg+C)} - E_{Hg} - Ec$, where $E_{(Hg+C)}$, $E_{Hg}$, $E_C$ are the total energies of the relaxed Hg+ $C_G$, Hg, and $C_G$ structures, respectively. The calculated total energy change for clusters consisting of 32-atom Hg particles and graphene sheets consisting of 112 atoms of C ($32Hg+112C_G$) is -0.14 eV/atom, indicating a strong interaction between the atoms of the Hg-particles and the C atoms of the graphene sheets (Figure S8 (a) – S8(c)). Taking a larger system consisting of 122-atom Hg particles and graphene sheets comprised of 240 C atoms ($122Hg+240C_G$) (Figure S8 (d)), we obtained a ΔE -0.11eV/atom. This suggests that the interactions between the Hg particle and graphene should occur regardless of the Hg-particle size. The calculated distance between $C_G$ and Hg is ~2.80 Å which is larger than the sum of the covalent radii of Hg and C(rc+ rhg =0.77 +1.49=2.26 Å) suggesting no covalent interaction between the Hg particle atoms and C atoms of graphene. The van der Waals (vdW) interactions between graphene and atoms of Hg particles leads to the buckling of graphene sheet (as can be seen in Figure S8) and causes deviation from the $sp^2$ hybridization which can enhance the interaction between graphene and Hg particles. To gain more insight into the strong interaction between Hg and graphene sheet, Bader changes analysis was carried out using the Bader analysis package [10] of Tang et al. and we have found that such a Hg-particle transfers 3 electrons (e) (0.096e/C-atom) and 5e (0.022e/C-atom) to the graphene sheet for $32Hg+112C_G$ (Figure S8(c)) and $122Hg+240C_G$ (Figure S8 (d)) structures, indicating that both ionic and vdWs interactions take place between the Hg-particles and the graphene sheets. The charge transfer from the Hg particle to the graphene sheet is further confirmed by calculating the accumulation and depletion of charge for the 122Hg+240$C_G$ structures as shown in Figure S8(d) and it is observed that the transferred electrons are mainly localized in the vicinity of the particle attached to the sheet. In the experimental work, we used RGO rather than graphene, which is expected to stabilize the Hg/C clusters much more. In our model, we have simulated 122 atoms of Hg particle on top of reduce graphene oxide (RGO) (12 oxygen and 3 hydrogen atoms were added to the graphene sheets to obtain 9 epoxy and 3 OH groups per 240 carbon atoms) (Figure S8 (e) and S8 (f)) to investigate the interaction between the Hg-particle and RGO. The relaxed structures of RGO and 122Hg+RGO are shown in Figure S8 (e) and S8 (f). The calculated ΔE becomes -0.22 eV/atom in each Hg/RGO cluster (altogether 377 atoms). Hence these calculations clearly indicate the much greater stability of the Hg/RGO clusters compared to the particles on bare graphene. The hydroxyl groups (2 OH groups out of 3 OH groups) near the particle break the single bond with the graphene and form a bond with the Hg particle. Epoxy groups (6 epoxy group out of 9 epoxy groups) break only one bond from graphene and act as bridge between the Hg-particle and graphene. At a distance of approximately 4 Å, all functional groups remain attached to the graphene sheet, indicating that the functional groups located far away from the Hg-particle must overcome a barrier to interact with the Hg-particle.

Analysis of the effect of the oxygen-containing groups on the graphene sheets shows that distance between the graphene ($C_G$) plane and the Hg particle is still ~2.80 Å, but more electrons can be transferred from the mercury particles (122 atoms each in the model) to the RGO compared to the unsubstituted graphene sheet: 10.95e (0.042e/atom (RGO)) transferred to the RGO from a Hg particle compared to the electron transfer to the pristine graphene of 5e (0.022e/C-atom). These electrons are mainly localized in the RGO in the vicinity of the Hg particle attached to the sheet. Moreover, without the contact with the Hg particle the graphene sheet should transfer 7.30e (0.03e/C) to the O-functional groups in the RGO sheets, whereas

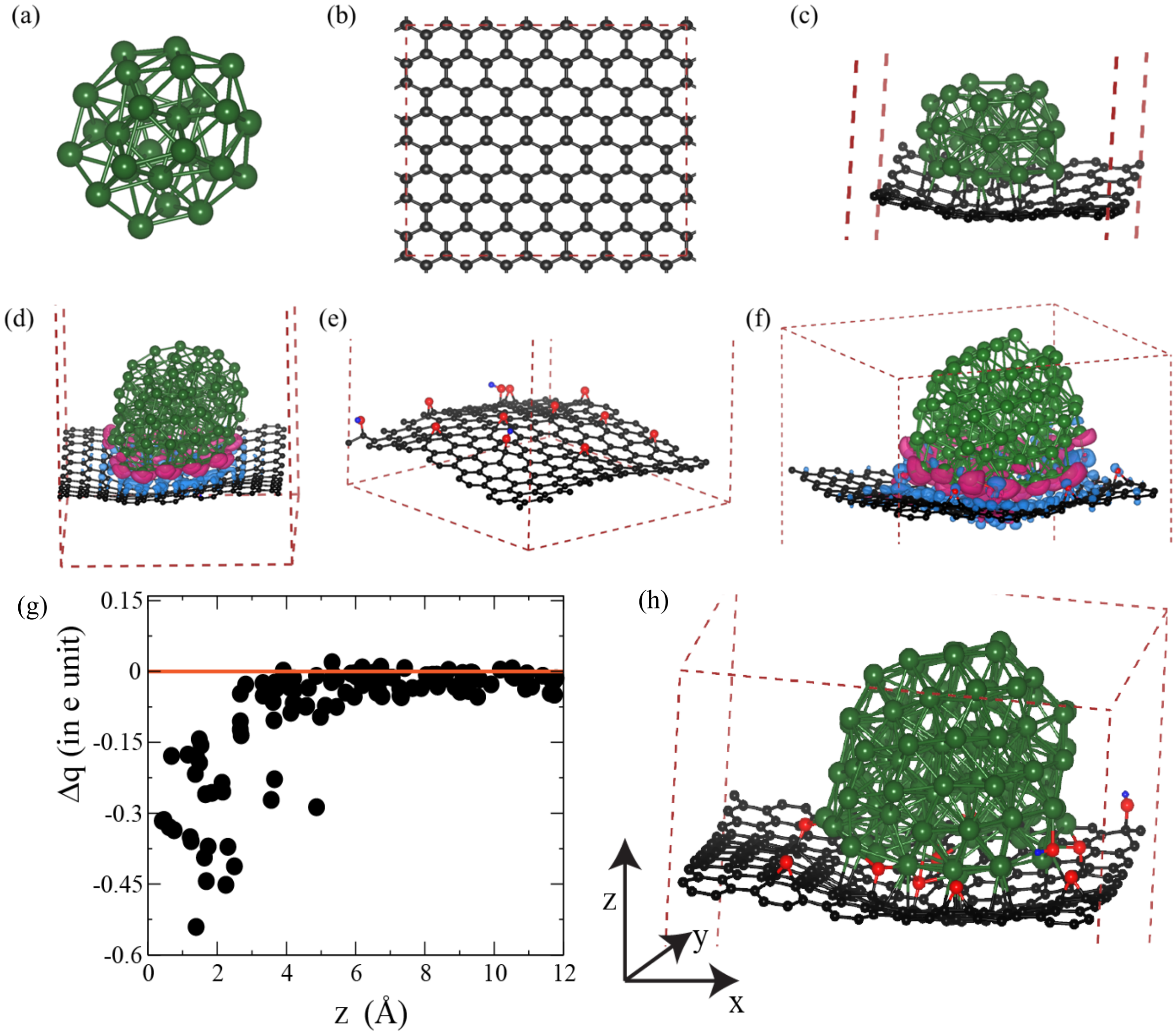

Figure S8. (a), (b), and (c) are relaxed structures with Hg particles consisting of 32 atoms, 240 C atoms (graphene supercell of 7x4x1) graphene sheet, and a 32-atom Hg particle on top of a 122- C atoms graphene sheet (32Hg-112$C_G$), respectively. Hg and C atoms are represented by green and black spheres. The Hg-C distance is ~ 2.80 Å. (d) Charge accumulation (shown by cyan colour) and depletion (represented by magenta colour) is shown for relaxed structure consisting of 122-atoms Hg particle and 240-atoms graphene sheet (122Hg+240$C_G$). The iso-surface value is set to 0.002 e/ Å$^3$, (e) relaxed structure of RGO comprised of 240 C atoms and 12 O atoms and 3 H atoms (9 epoxy groups and 3 OH groups per 240 C atoms of graphene sheet). (f) a relaxed structure constituted of 122-atoms Hg particle and RGO (122Hg+RGO). Hg, C, O and H atoms are shown by green, black, red and blue spheres, respectively. Doted solid maroon colour lines represent cell boundaries. (g) and (h) charge depletion of Hg particle to RGO sheet as function of z-coordinate of the Hg atoms. The charge depletion calculated as $\Delta q = q(z)_{Hg\ (on\ RGO)} - q(z)_{Hg(free\ standing\ )}$, Where, q is Bader charge. Minimum distance of Hg atoms from the RGO sheet is set to zero. The charge of the Hg atoms up to 5.0 Å from RGO sheet is significantly depleted whereas above 4.0 Å average layer charge of Hg atoms show slight change.

for the RGO+Hg case, the graphene sheet receives 1.36e (0.006e/C) through the oxygenated functional groups. This indicates that the graphene sheets in the model gain 8.66e (0.036e/C) each, owing to the contact with the mercury particles. Such a charge transfer from the Hg atoms in the particles to the functional graphene moieties should create ionic interactions between the Hg particles and the graphene sheets, together with obvious Van-der-Waals (vdW) interactions. In the presence of oxygenated functional groups on the carbon planes (using RGO), the partial charge transfer interactions between the Hg particles and the partially oxygenated graphene sheets along with the vdW interactions are enhanced further. Studies of both systems confirm that the electronic interactions with a slight charge transfer between the mercury (donor) and the graphene (acceptor) leads to the stabilization of the mercury nano-particles attached to the RGO, enable them to remain solid even at elevated temperatures above RT. Such interactions which lead to electrical polarization (the mercury is slightly positively charged while the contacting RGO is slightly negatively charged), explain well the relatively high melting point of these HgNPs.

The quantified charge transfer of Hg atoms to RGO sheet is shown in the Figure S8. The calculated results reveal that up to 3rd layer of Hg, there is less than -0.1e charge transfer to RGO sheet and average charge transfer above 3rd layer of Hg atoms to RGO is weak. The average Hg-Hg bond distance is calculated by considering a cut off radius 3.5 Å and found no considerable change of Hg-Hg bond length between Hg particle on RGO and free-standing Hg particle.

Here, we provide a further clarification about the mechanism of the formation of solid Hg nanoparticles. Sonication plays a key role in nano dispersion, formation of nano Hg droplets which are thrown towards the RGO sheets and interact with their surface via a partial charge transfer. These interactions induce the crystallization of the nano Hg droplets and the crystalline solid HgNPs thus formed are stabilized by the RGO (cage type structure). The nano-dispersed mercury droplets during the sonication process are compressed onto the RGO and undergo electronic interactions with the RGO. Such embedding of small particles is in fact well-known in the sonochemistry literature. It is well documented that the collapse of the acoustic bubbles near solid surfaces leads to the formation of liquid microjets directed towards the solid surface and throws the NPs at a speed of > 500 m/sec onto the substrate, leading to the stable embedding of the nanoparticles.

For instance, in the case of CuO particles coated on cotton, after the fabric has undergone 65 washing cycles at 75 °C, 83% of the particles were still found on the fabric, because the CuO particles shift the polymeric chains and are well embedded in the fabric. In an another case of Ag NPs interacting with glass by sonic energy in solution, Ag NPs were found by TOFSIMS measurements to be embedded as deep as 60-80 nm into the glass. Therefore, the embedding of Hg droplets into the carbonaceous matrices due to high energy deposition and strong interactions with these matrices is highly consistent with previous work.[11,12]

For substantiating this mechanism, we have conducted the synthesis of HgNPs on several different types of carbon moieties (graphite, graphitized graphene, graphene oxide, CNT) that can also interact similarly with Hg nano-droplets. We identified formation of SSHg nanoparticles in several composites including graphene oxide (we have not included these studies in the present manuscript).

***UV-VIS reflectance spectroscopy:***

The optical properties of the HgNPs were explored by measuring the absorbance of the particles using UV-VIS reflectance spectrometry. Thin films of HgNPs samples were prepared by dispersing the powdered sample in ethanol and drop casting on glass slides. Their spectrum is presented in Figure S9, curve (ii), showing an absorption peak at $\lambda_{max}$ ~ 284 nm assigned to the nanoscale solid mercury particles, whereas, the peak at $\lambda_{max}$ ~ 254 nm is attributed to the RGO absorption. The latter peak matches well with the bare RGO in Figure S9, curve (i).

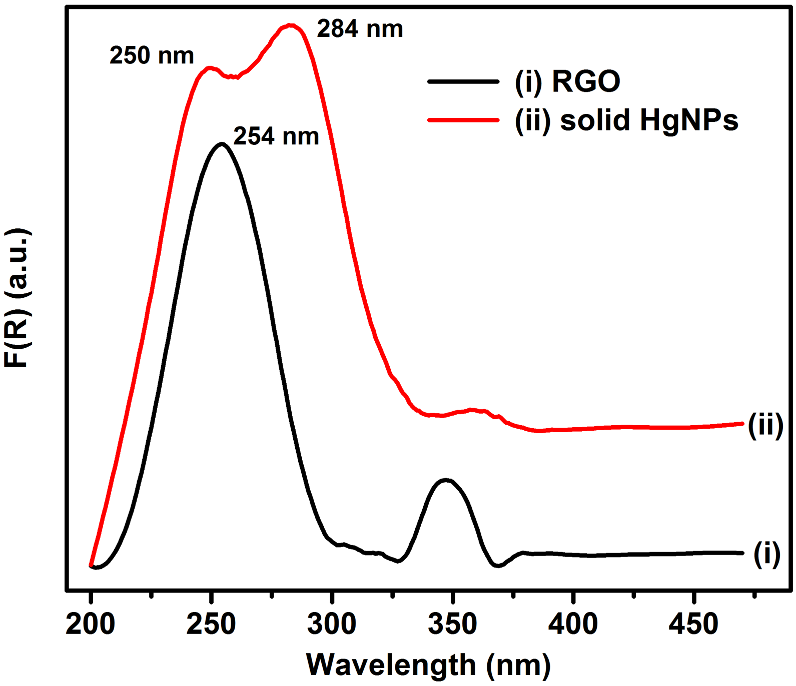

Figure S9. UV-Vis reflectance spectra of bare RGO (curve (i)) and Hg NPs (curve (ii)).

### *FTIR and Raman spectroscopic studies for RGO and Solid HgNPs*

Figure S10 (a) and S10 (b) represents the FTIR spectra and Raman spectra of RGO curve (i) and Solid HgNPs curve (ii), respectively. Both the FTIR Curves (Figure S10 (a)) appear more or less similar indicating no change in the functional group after the formation of Hg nanoparticles on the RGO, indicating that these functional groups are not participating in the bonding with Hg, however, these functional groups help in stabilizing the formed Hg nanoparticles on RGO through the charge transfer mechanism. Similarly, in the Raman spectra (Figure S10 (b)) both curves of RGO (curve (i)) and HgNPs (curve (ii)) showing intensity ratio of the D and G band ($I_D/I_G$) has no much significant. The slight increase in case of HgNPs sample may be due exposure of RGO to 1 hour sonication which might have increased the defects.

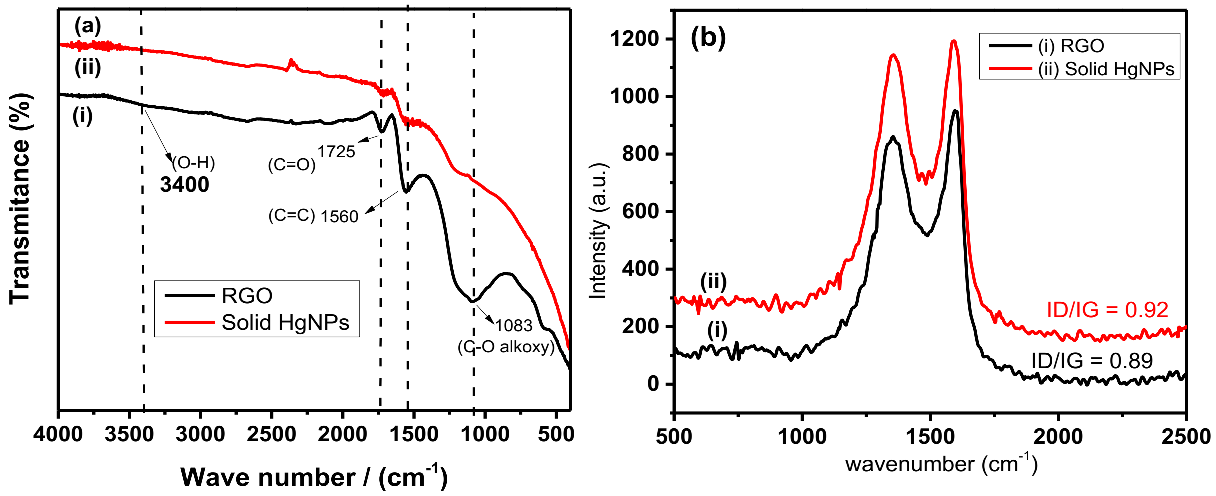

Figure S10. FTIR (a) and Raman spectra (b) for RGO and HgNPs

***FTIR spectroscopic analysis of Graphite, Graphite oxide and RGO:***

The FTIR spectra of graphite, GO and RGO samples are shown in Figure S11. Curve (ii), in this figure shows a broad absorption band at 3400 cm$^{-1}$ due to the presence of O-H groups on the graphene oxide surface. The bands at 1723 and 1605 cm$^{-1}$ correspond to C=O and C=C bond stretching, respectively [13–17]. The peaks at 1204, 1038 and 1384 cm$^{-1}$ represent the stretching of C-O (epoxy), C-O (alkoxy) and the deformation peak of O-H group, respectively. In the spectra of RGO (Figure S11, curve iii), disappearance of absorption bands at 3250 and 1723 cm$^{-1}$ (C=O) confirms the reduction of graphite oxide to reduced graphene oxide.

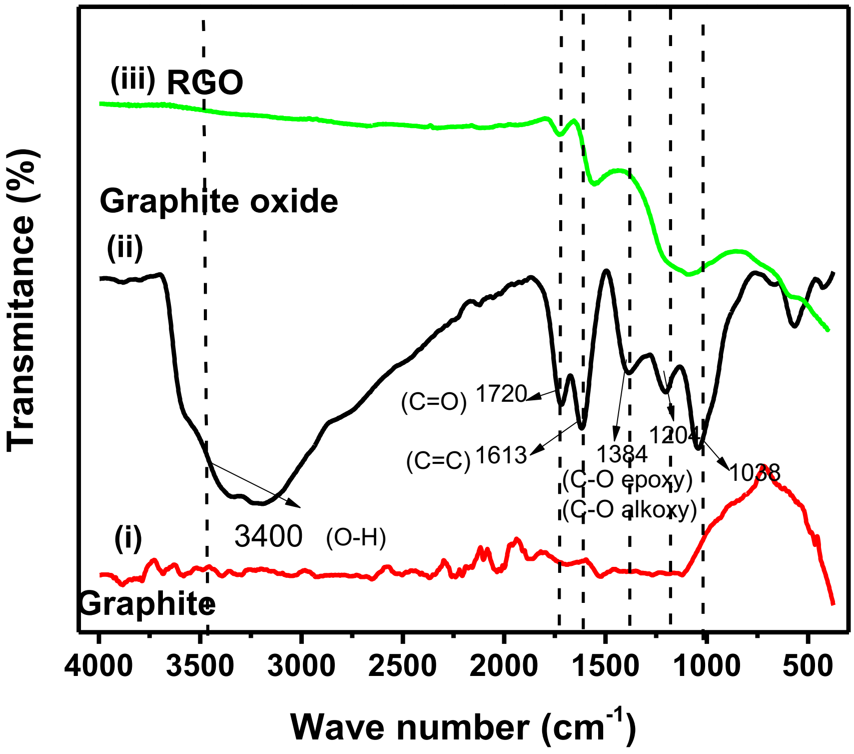

Figure S11. FTIR spectra of graphite (i), GO (ii), RGO (iii).

### *XPS analysis of Graphite, Graphite oxide and RGO:*

The X-ray photoelectron C1s spectra (XPS) of graphite, GO and RGO samples are shown in Figure S12 (a), which identify their surface chemistry. Figure S12 (b), S12 (c) show the de-convoluted C1s spectra of GO and RGO, respectively. These spectra are fitted to Gaussian-Lorentzian curves after Shirley background correction. The C1s de-convoluted spectrum for GO (Figure S12 (b)) shows four characteristic peaks at 284.5, 285.3, 286.6 and 288.8 eV for $sp^2$ hybridized C, $sp^3$ hybridized C, epoxy, carboxyl and carbonyl groups, respectively [13–17]. After thermal reduction of GO to reduced graphene oxide, the $sp^3$ C-C peak intensity decreased and $sp^2$ C=C peak intensity increased. Thus, the XPS confirms the formation of oxygen functional groups in case of GO and reduction of these functional groups after thermal exfoliation for the RGO sample.

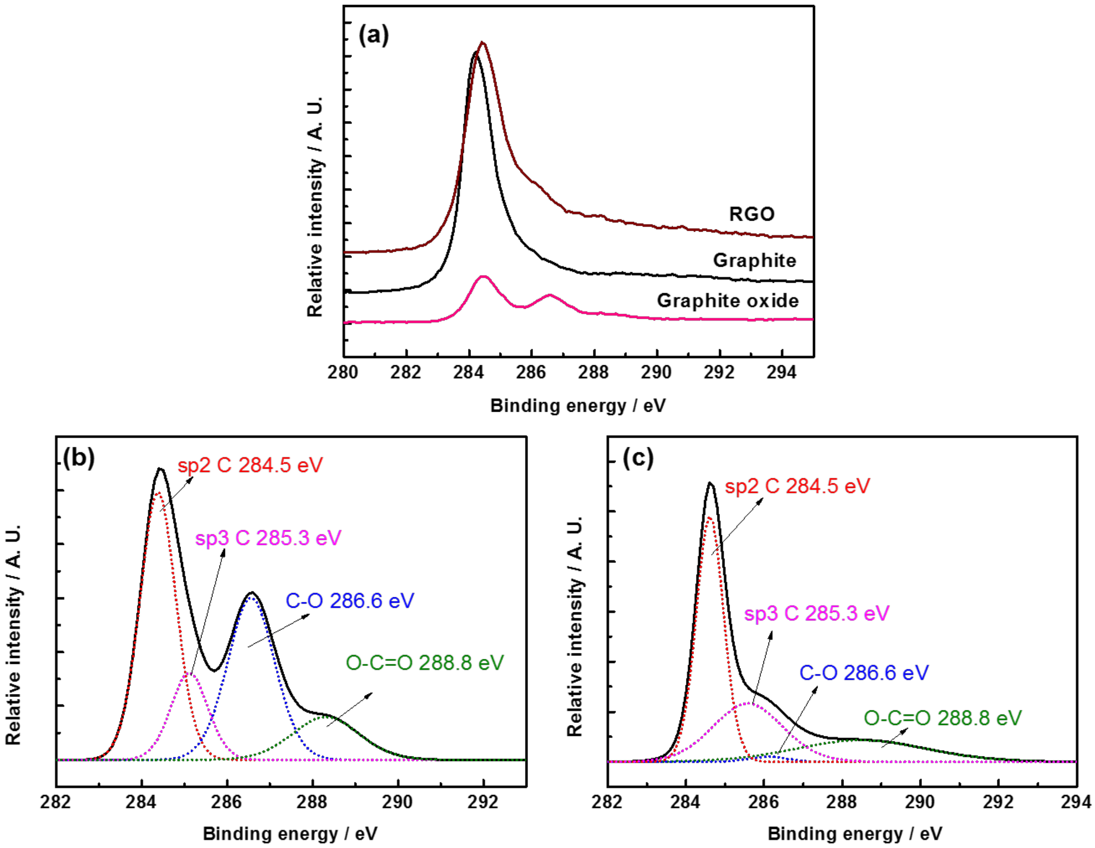

Figure S12. XPS (a) C1s peaks of Graphite (i), GO (ii), RGO (iii) and de-convoluted C1s spectra of (b) GO and (c) RGO.

***Raman spectroscopic analysis of Graphite, Graphite oxide and RGO:***

The thermal reduction is further examined by Raman spectra (Figure S13). The Raman spectra provide D and G bands at 1347 and 1580 cm$^{-1}$ and are assigned to disorder and local defects. [14–17] In the RGO samples' spectra, the G band shows a shift to 1588 from 1570 cm$^{-1}$ (the value for pristine graphite), indicating the reduction of GO. Simultaneously, the intensity of the D band has increased, and the G band has broadened compared to graphite. The intensity ratio of the D and G band ($I_D/I_G$) has increased. It is mainly due to the defects caused by the removal of carbon and oxygen during the thermal decomposition.

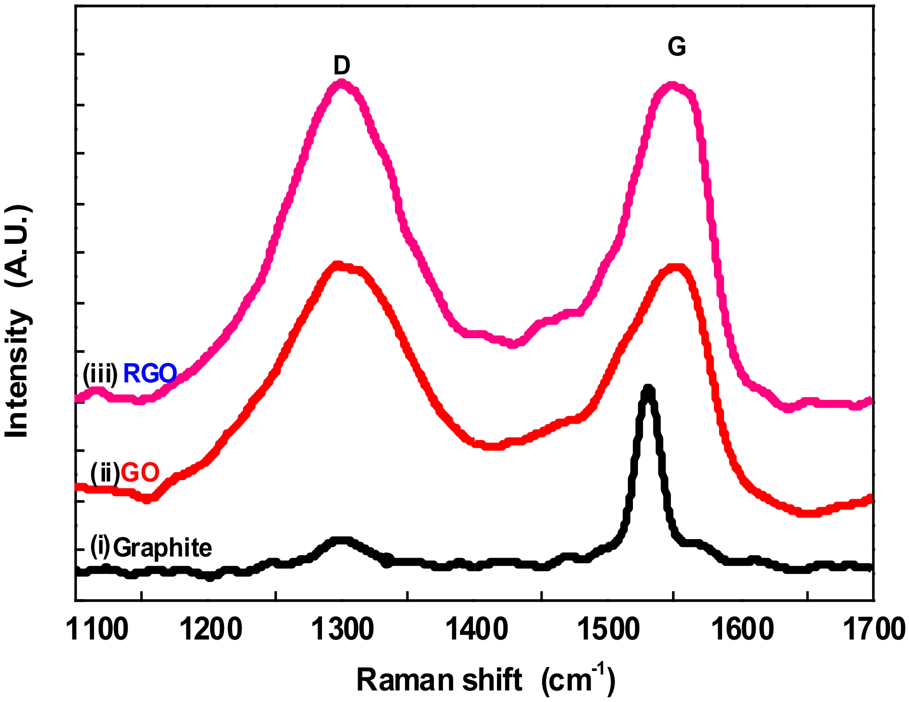

Figure S13. Raman spectra of (i) graphite, (ii) GO, (iii) RGO.

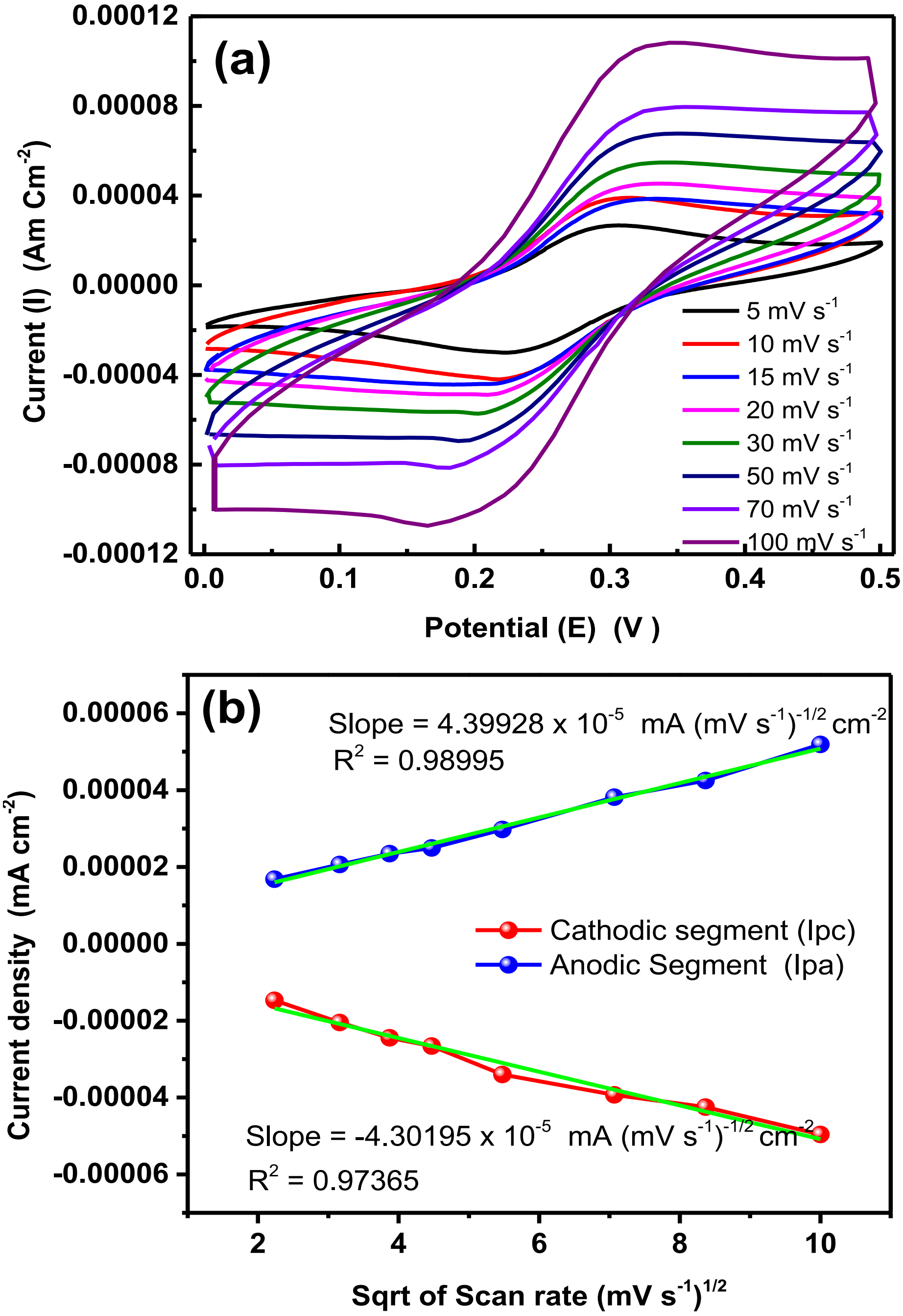

Figure S14. (a) Cyclic voltammograms and (b) Randles-Sevcik plots of the linear dependence of the anodic and cathodic peak current values vs. the square root of the scan rate for bare GCE in 2 mM $K_4[Fe(CN)_6]/K_3[Fe(CN)_6]$ mixed with 8 ml of 1M KCl, recorded at different scan rates from 5 to 100 mV $s^{-1}$ with a potential window between 0.0 and 0.50 V vs Ag/AgCl.

Table S2. Electrochemical parameters obtained from the voltammograms of Figure S14 for bare GCE

| Working electrode : Bare GCE | | | | | | |
|---|---|---|---|---|---|---|
| **Scan rate mV $s^{-1}$** | **Epa** | **Epc** | **Ipa** | **Ipc** | **Ipa/Ipc** | **Epa-Epc=Ep** |
| **5** | 0.306 | 0.22 | $1.680E^{-5}$ | $-1.470E^{-5}$ | $-1.14E^{+00}$ | 0.086 |
| **10** | 0.309 | 0.22 | $2.065E^{-5}$ | $-2.050E^{-5}$ | $-1.01E^{+00}$ | 0.089 |
| **15** | 0.323 | 0.21 | $2.346E^{-5}$ | $-2.445E^{-5}$ | $-9.60E^{-01}$ | 0.113 |
| **20** | 0.327 | 0.21 | $2.495E^{-5}$ | $-2.662E^{-5}$ | $-9.37E^{-01}$ | 0.117 |
| **30** | 0.3286 | 0.203 | $2.974E^{-5}$ | $-3.400E^{-5}$ | $-8.75E^{-01}$ | 0.1256 |
| **50** | 0.336 | 0.19 | $3.816E^{-5}$ | $-3.930E^{-5}$ | $-9.71E^{-01}$ | 0.146 |
| **75** | 0.335 | 0.18 | $4.25E^{-5}$ | $-4.250E^{-5}$ | $-1.00E^{+00}$ | 0.155 |
| **100** | 0.339 | 0.166 | $5.188E^{-5}$ | $-4.960E^{-5}$ | $-1.05E^{+00}$ | 0.173 |

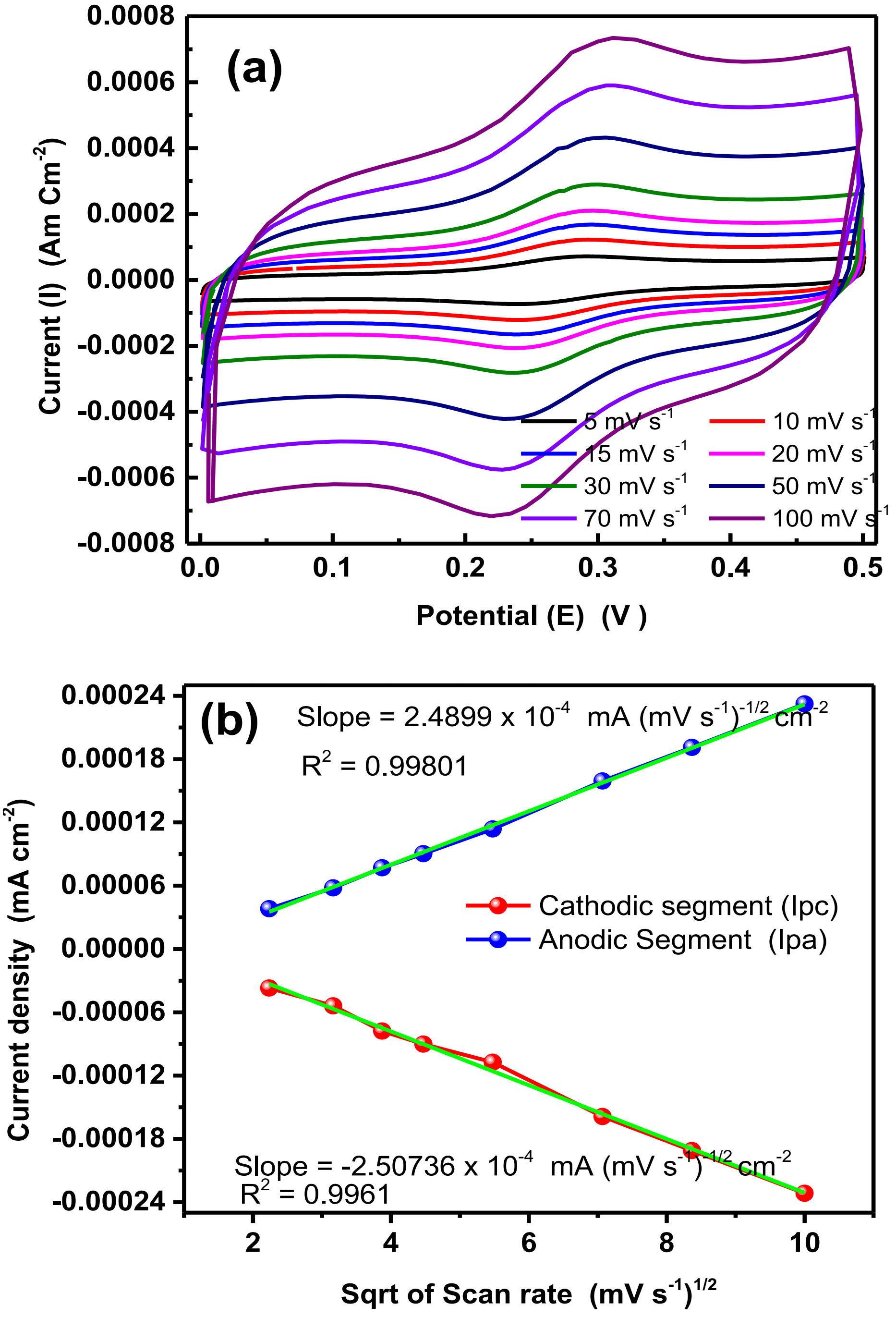

Figure S15. (a) Cyclic voltammograms and (b) Randles-Sevcik plots of linear dependence of the anodic and cathodic peak current values against the square root of the scan rate for RGO/GCE in 2 mM $K_4[Fe(CN)_6]/K_3[Fe(CN)_6]$ mixed with 8 ml of 1M KCl aqueous solutions recorded at different scan rates from 5 to 100 mV s$^{-1}$ with a potential window between 0.0 and 0.50 V vs Ag/AgCl.

Table S3. Electrochemical parameters obtained from voltammograms of Figure S15 for RGO/GCE

| **Working electrode : RGO/GCE** | | | | | | |
|---|---|---|---|---|---|---|
| **Scan rate mV s$^{-1}$** | **Epa** | **Epc** | **Ipa** | **Ipc** | **Ipa/Ipc** | **Epa-Epc=Ep** |
| **5** | 0.292 | 0.239 | 3.813E$^{-5}$ | -3.705E$^{-5}$ | -1.03E$^{+00}$ | 0.053 |
| **10** | 0.293 | 0.240 | 5.798E$^{-5}$ | -5.400E$^{-5}$ | -1.07E$^{+00}$ | 0.053 |
| **15** | 0.295 | 0.240 | 7.698E$^{-5}$ | -7.780E$^{-5}$ | -0.99E$^{+00}$ | 0.055 |
| **20** | 0.296 | 0.239 | 9.040E$^{-5}$ | -9.024E$^{-5}$ | -1.00E$^{+00}$ | 0.057 |
| **30** | 0.300 | 0.236 | 11.38E$^{-5}$ | -10.74E$^{-5}$ | -1.06E$^{+00}$ | 0.064 |
| **50** | 0.306 | 0.229 | 15.93E$^{-5}$ | -15.89E$^{-5}$ | -1.00E$^{+00}$ | 0.077 |
| **75** | 0.310 | 0.228 | 19.12E$^{-5}$ | -19.11E$^{-5}$ | -1.00E$^{+00}$ | 0.082 |
| **100** | 0.311 | 0.219 | 23.24E$^{-5}$ | -23.17E$^{-5}$ | -1.00E$^{+00}$ | 0.092 |

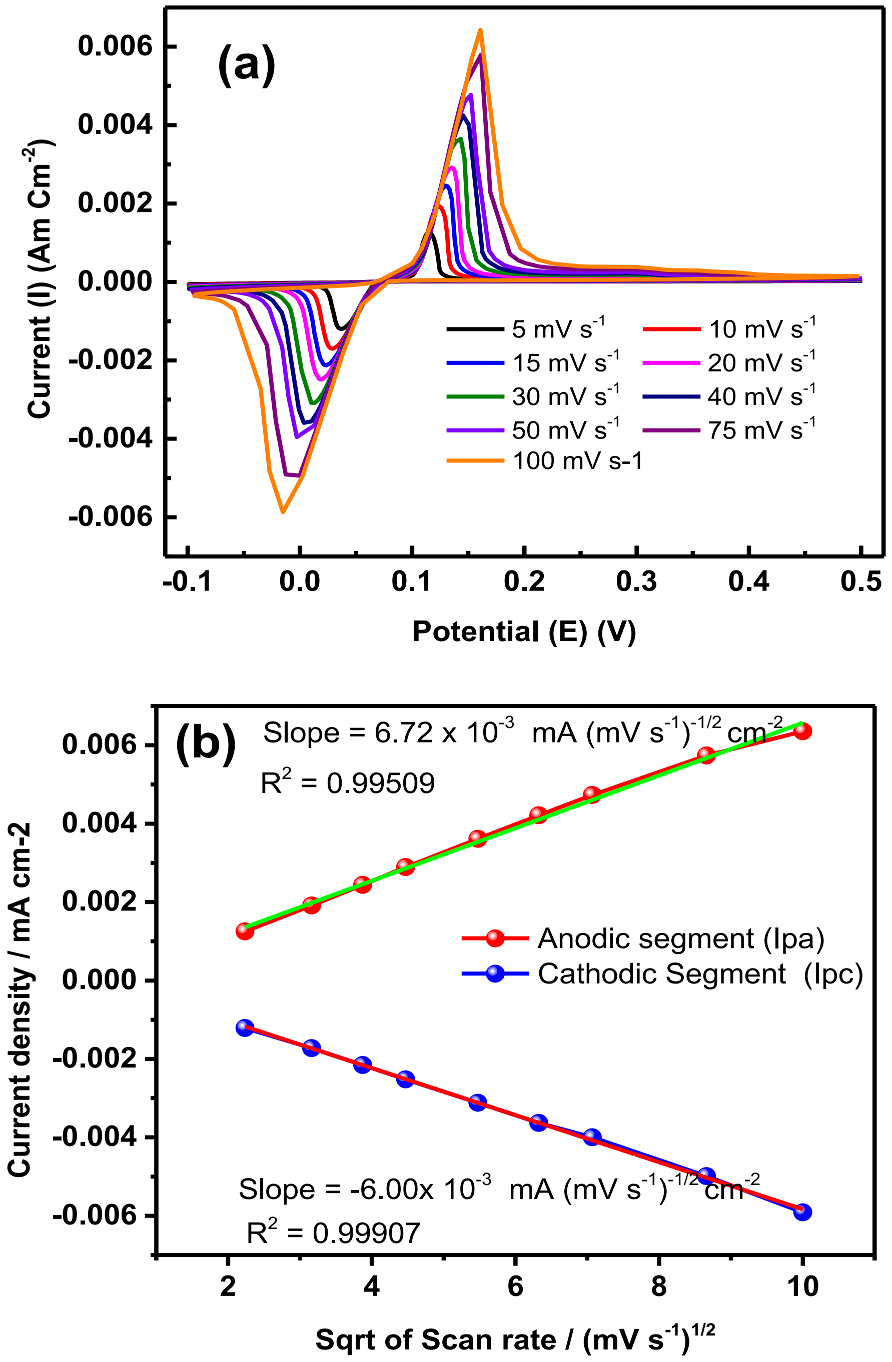

Figure S16. (a) Cyclic voltammograms and (b) Randles-Sevcik plots of linear dependence of the anodic and cathodic peak current values vs. the square root of the scan rate for Hg/GCE in 2 mM $K_4[Fe(CN)_6]/K_3[Fe(CN)_6]$ mixed with 8 ml of 1M KCl aqueous solutions recorded at different scan rates from 5 to 100 mV s$^{-1}$ with a potential window between 0.0 and 0.50 V vs Ag/AgCl.

Table S4. Electrochemical parameters obtained from the voltammograms of Figure S16 for Hg/GCE

| **Working electrode : Hg/GCE** | | | | | | |
|---|---|---|---|---|---|---|
| **Scan rate mV s$^{-1}$** | **Epa** | **Epc** | **Ipa** | **Ipc** | **Ipa/Ipc** | **Epa-Epc=Ep** |
| **5** | 0.115 | 0.0363 | 12.523E$^{-4}$ | -12.123E$^{-4}$ | -1.03E$^{+00}$ | 0.0787 |
| **10** | 0.124 | 0.0285 | 19.115E$^{-4}$ | -17.238E$^{-4}$ | -1.11E$^{+00}$ | 0.0955 |
| **15** | 0.130 | 0.023 | 24.391E$^{-4}$ | -21.545E$^{-4}$ | -1.13E$^{+00}$ | 0.107 |
| **20** | 0.135 | 0.0197 | 28.909E$^{-4}$ | -25.220E$^{-4}$ | -1.15E$^{+00}$ | 0.1153 |
| **30** | 0.143 | 0.0133 | 36.143E$^{-4}$ | -31.193E$^{-4}$ | -1.16E$^{+00}$ | 0.1297 |
| **40** | 0.145 | 0.0037 | 42.122E$^{-4}$ | -36.343E$^{-4}$ | -1.16E$^{+00}$ | 0.1413 |
| **50** | 0.152 | 0.0028 | 47.310E$^{-4}$ | -39.995E$^{-4}$ | -1.18E$^{+00}$ | 0.1492 |
| **75** | 0.161 | 0.0003 | 57.397E$^{-4}$ | -49.879E$^{-4}$ | -1.15E$^{+00}$ | 0.1607 |
| **100** | 0.161 | 0.00015 | 63.539E$^{-4}$ | -59.134E$^{-4}$ | -1.03E$^{+00}$ | 0.0787 |

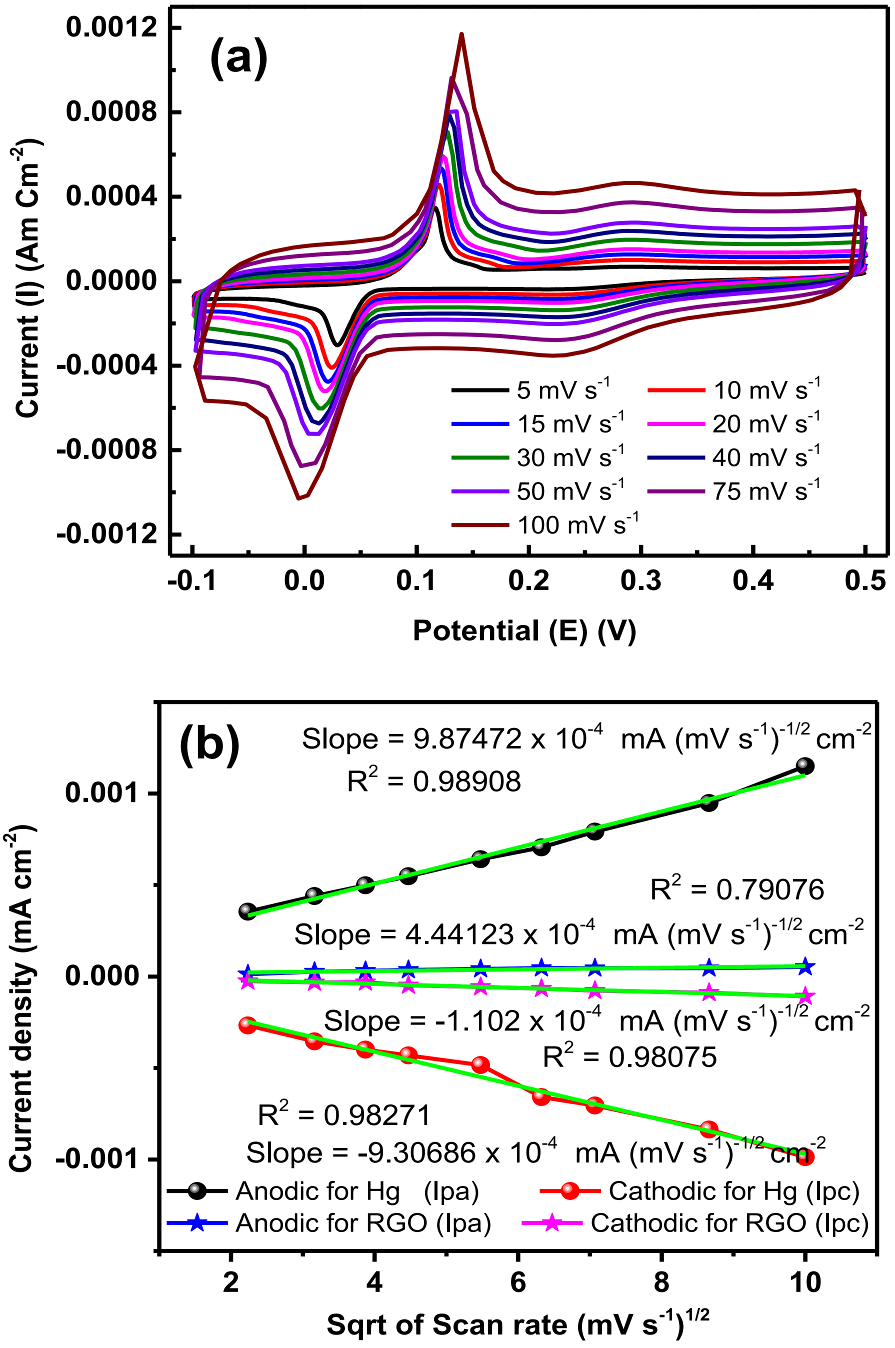

Figure S17. (a) Cyclic voltammograms and (b) Randles-Sevcik plots of linear dependence of the anodic and cathodic peak current values vs. the square root of the scan rate for solid HgNPs/GCE in 2 mM $K_4[Fe(CN)_6]/K_3[Fe(CN)_6]$ mixed with 8 ml of 1M KCl aqueous solutions recorded at different scan rates from 5 to 100 mV s$^{-1}$ with a potential window between 0.0 and 0.50 V vs Ag/AgCl.

Table S5. Electrochemical parameters obtained from the voltammograms of Figure S17 for solid HgNPs/GCE, low redox region is for HgNPs and high redox region is for RGO.

**Working electrode : HgNPs/GCE for Hg nanoparticles**

| Scan rate mV s$^{-1}$ | Epa | | Epc | | Ipa | | Ipc | | Ipa/Ipc | | Epa-Epc=Ep | |
|---|---|---|---|---|---|---|---|---|---|---|---|---|
| | HgNps | RGO | HgNps | RGO | HgNps | RGO | HgNps | RGO | HgNps | RGO | HgNps | RGO |
| **5** | 0.116 | 0.291 | 0.0295 | 0.218 | 3.54E$^{-4}$ | 1.2E$^{-5}$ | -2.67E$^{-4}$ | -2.48E$^{-5}$ | -1.33E$^{+00}$ | -4.84E$^{-01}$ | 0.0865 | 0.073 |
| **10** | 0.120 | 0.291 | 0.0238 | 0.219 | 4.40E$^{-4}$ | 2.66E$^{-5}$ | -3.54E$^{-4}$ | -3.19E$^{-5}$ | -1.24E$^{+00}$ | -8.34E$^{-01}$ | 0.0962 | 0.072 |
| **15** | 0.122 | 0.29 | 0.0210 | 0.223 | 4.99E$^{-4}$ | 3.14E$^{-5}$ | -4.00E$^{-4}$ | -3.084E$^{-5}$ | -1.25E$^{+00}$ | -1.02E$^{+00}$ | 0.101 | 0.067 |
| **20** | 0.123 | 0.29 | 0.0198 | 0.224 | 5.48E$^{-4}$ | 3.598E$^{-5}$ | -4.31E$^{-4}$ | -4.778E$^{-5}$ | -1.27E$^{+00}$ | -7.53E$^{-01}$ | 0.1032 | 0.066 |
| **30** | 0.128 | 0.29 | 0.0159 | 0.226 | 6.41E$^{-4}$ | 4.119E$^{-5}$ | -4.84E$^{-4}$ | -5.631E$^{-5}$ | -1.32E$^{+00}$ | -7.31E$^{-01}$ | 0.1121 | 0.064 |
| **40** | 0.129 | 0.29 | 0.0127 | 0.224 | 7.06E$^{-4}$ | 4.689E$^{-5}$ | -6.59E$^{-4}$ | -6.579E$^{-5}$ | -1.07E$^{+00}$ | -7.13E$^{-01}$ | 0.1163 | 0.066 |
| **50** | 0.130 | 0.29 | 0.0127 | 0.225 | 7.92E$^{-4}$ | 4.603E$^{-5}$ | -7.05E$^{-4}$ | -7.739E$^{-5}$ | -1.12E$^{+00}$ | -5.95E$^{-01}$ | 0.1173 | 0.065 |
| **75** | 0.131 | 0.29 | 0.0098 | 0.225 | 9.48E$^{-4}$ | 4.589E$^{-5}$ | -8.36E$^{-4}$ | -8.862E$^{-5}$ | -1.13E$^{+00}$ | -5.18E$^{-01}$ | 0.1212 | 0.065 |
| **100** | 0.140 | 0.29 | 0.0017 | 0.221 | 11.50E$^{-4}$ | 5.242E$^{-5}$ | -9.87E$^{-4}$ | -1.084E$^{-4}$ | -1.17E$^{+00}$ | -4.84E$^{-01}$ | 0.1383 | 0.069 |

Table S6. Calculated diffusion coefficients for the reaction of the $Fe(CN)_6^{4-/3-}$ red-ox couple on the 4 electrodes.

| Electrode | Slope (mA (mV $s^{-1}$)$^{-1/2}$ $cm^{-2}$) | | Diffusion coefficient ($cm^2$ $s^{-1}$) | |
|---|---|---|---|---|
| | **Cathodic** | **Anodic** | **Cathodic** | **Anodic** |
| **GCE** | -4.30 x $10^{-5}$ | 4.40 x $10^{-5}$ | 8.30 x $10^{-7}$ | 8.70 x $10^{-7}$ |
| **RGO** | -2.51 x $10^{-4}$ | 2.49 x$10^{-4}$ | 2.90 x $10^{-6}$ | 2.80 x $10^{-6}$ |
| **Hg** | -6.00 x $10^{-3}$ | 6.72 x $10^{-3}$ | 1.55 x $10^{-5}$ | 1.95 x $10^{-5}$ |
| **HgNPs** | -9.31 x $10^{-4}$ | 9.90 x $10^{-4}$ | 3.70 x $10^{-5}$ | 4.20 x $10^{-5}$ |

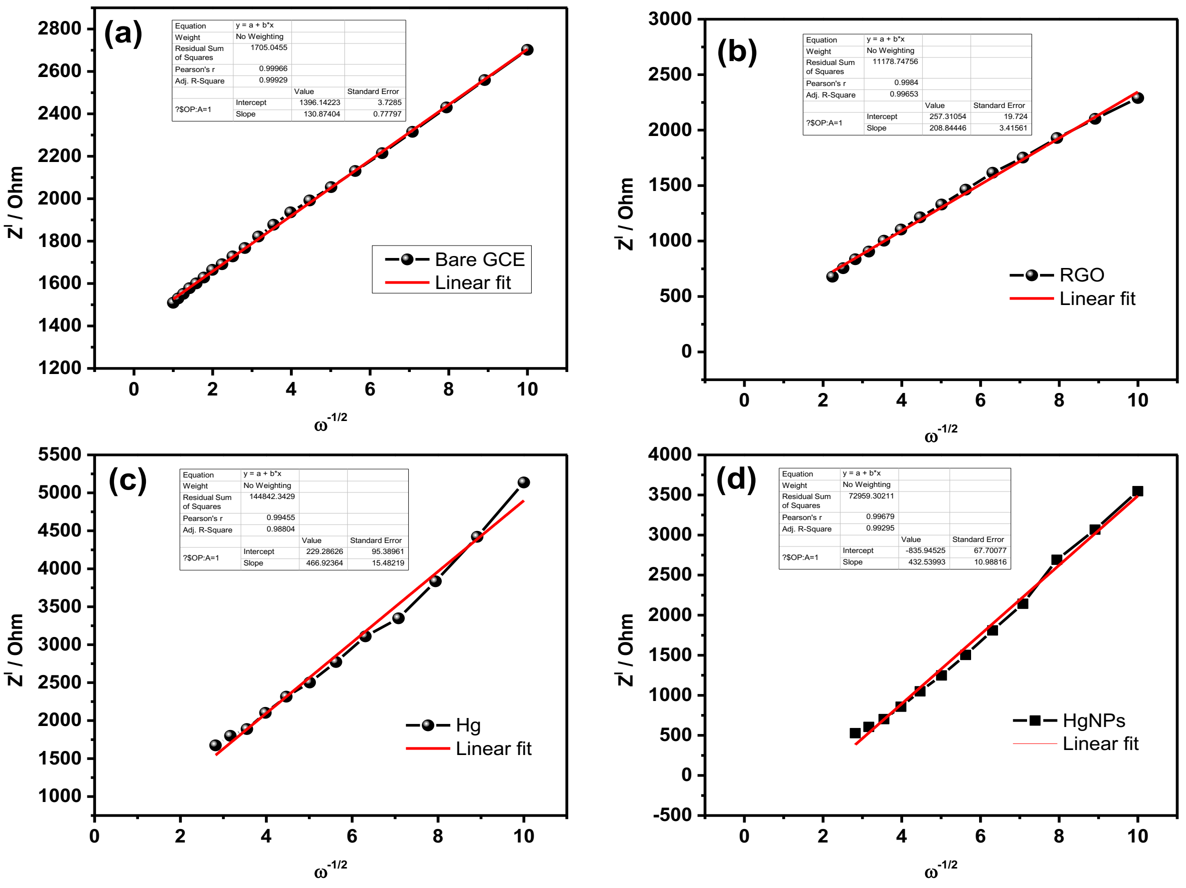

(a)

| Equation | y = a + b*x | | |
|---|---|---|---|
| Weight | No Weighting | | |
| Residual Sum of Squares | 1705.0455 | | |
| Pearson's r | 0.99966 | | |
| Adj. R-Square | 0.99929 | | |
| | | Value | Standard Error |
| ?$OP:A=1 | Intercept | 1396.14223 | 3.7285 |
| | Slope | 130.87404 | 0.77797 |

(b)

| Equation | y = a + b*x | | |
|---|---|---|---|
| Weight | No Weighting | | |
| Residual Sum of Squares | 11178.74756 | | |
| Pearson's r | 0.9984 | | |
| Adj. R-Square | 0.99653 | | |
| | | Value | Standard Error |
| ?$OP:A=1 | Intercept | 257.31054 | 19.724 |
| | Slope | 208.84446 | 3.41561 |

(c)

| Equation | y = a + b*x | | |
|---|---|---|---|
| Weight | No Weighting | | |
| Residual Sum of Squares | 144842.3429 | | |
| Pearson's r | 0.99455 | | |
| Adj. R-Square | 0.98804 | | |
| | | Value | Standard Error |
| ?$OP:A=1 | Intercept | 229.28626 | 95.38961 |
| | Slope | 466.92364 | 15.48219 |

(d)

| Equation | y = a + b*x | | |
|---|---|---|---|
| Weight | No Weighting | | |
| Residual Sum of Squares | 72959.30211 | | |
| Pearson's r | 0.99679 | | |
| Adj. R-Square | 0.99295 | | |
| | | Value | Standard Error |
| ?$OP:A=1 | Intercept | -835.94525 | 67.70077 |
| | Slope | 432.53993 | 10.98816 |

Figure S18. The low frequency domains of the impedance spectra, presented as Nyquist plots, of (a) bare GCE, (b) RGO/GCE, (c) Hg/GCE and (d) HgNPs/GCE electrodes in 2 mM $K_4[Fe(CN)_6]/K_3[Fe(CN)_6]$ mixed with 8 ml of 1M KCl aqueous solutions. These domains of the impedance spectra can be fitted as nearly linear responses (see the fittings in red).

**Discussion on the significance of the calculated diffusion coefficient values (table)**

As seen in Table S6, the diffusion coefficient for the cathodic and anodic reaction of the $Fe(CN)_6^{4-/3-}$ red-ox couple GC, RGO/GC on the four electrodes are comparable, demonstrating the reversible nature of these reactions (as suggested). The significance of the calculated values of the diffusion coefficient cannot be discussed on the quantitative level, because the actual relevant active surface area of these electrodes is not clear. Hence, these values can only be discussed on the qualitative level. The RGO/GC electrodes are supposed to have much higher specific area than the GC electrodes, which explains their higher diffusion coefficient. In turn, the Hg/GC electrodes also have relatively small specific area (should be close to the geometric value), yet the relevant diffusion coefficient value is nearly 20 times higher than that related to GC electrodes (despite the fact that both are supposed to have similar active surface area) and 5 times higher than that of the RGO/GC electrodes, whose specific surface area should be much higher than that of the Hg/GC electrodes due to the nanostructure of the RGO. The only way to explain these differences is by suggesting that the Hg surface affinity and suitability for a smooth, simple electrochemical reaction is much greater than that of both GC and RGO. Despite the high specific surface area of the RGO, it is quite possible that it is a poor electrode material since only a small portion of its sites are interacting electrochemically. Further investigation of the electrochemical differences among these materials is far beyond the scope of this paper, because their electrochemical behavior is important here only as a background for the response of the HgNPs/GC electrodes. The fact that the diffusion coefficient calculated for them is the highest (e.g. nearly 10 and 2 times higher compared that of RGO/GC and Hg/GC electrodes respectively), despite the small amount of solid HgNPs on the electrodes is important. This finding seems to indicate that the solid Hg nanoparticles confined within the RGO sheets have clear electro-catalytic activity.

Table S7. Literature survey of metal nanoparticles for HER in 0.5M $H_2SO_4$

| **Material** | **Morphology** | **$\eta$0 (mV)** | **$\eta$ 10 (mV)** | **Tafel slop (mV dec$^{-1}$)** | **Reference** |
|---|---|---|---|---|---|
| Pt | Nanoparticle | | | 33 to 40 | [22–32] |
| Au/Graphene quantum dots (Au-GQDT) | Nanoparticles | 140 (Au-GQDT)<br>270 (Au NPS) | | 75 (Au-GQDT)<br>78 (Au NPS) | [23] |
| Au/N-doped carbon | | 54 | | 77 | [24] |
| Pd/RGO | | | | 46 | [25] |
| Pd/RGO | | 380 | | 122 | [26] |
| HCP Ru/N-carbon -400 oC preparation temperature | Nanoparticles | | | 114 | [27] |
| Ru/N-carbon shell | Nanoparticle | | 152 | 92.2 | [28] |
| Co | Nanoparticle | 14 | | 94 | [29] |
| Ni | nanoparticle | | | 98 | [30] |
| Ni-WN | Nanowire<br>(1.0 M KOH) | | | 71 | [31] |
| Cu/Carbon nanofibers | Nanoparticle | | 200 | 152 | [32] |
| **Hg** | **Nanoparticle** | **472** | **520** | **105** | **Present work** |

***XRD analysis:***

The X-ray diffraction patterns of graphite, graphite oxide (GO), reduced graphene oxide (RGO) samples are shown in Figure S19. Graphite (Figure S19, curve (i)) shows characteristic peak at $2\theta = 26.5^{o}$, corresponding to (002) reflection of hexagonal graphite structure. The inter-layer distance of (002) plane obtained for graphite is 3.38 Å. This value is comparable with the reported values [20,23]. Curve ii in Figure S19 represents the diffraction pattern of GO where we observe the shift in (002) reflection from $26.5^{o}$ to $10.3^{o}$, due to an increase in inter-layer distance (8.48 Å). After reduction of GO the shifted (002) plane reappears near to $26.5^{o}$ and is characterized by the low intensity, broad (002) reflection of RGO (Figure S19, curve (iii)). This is due to a disturbance in the regular stacking of GO that makes diffraction peaks weak or even disappear [13,33,34]. The breadth of the peak is attributed to smaller sheet size ($\leq 1$ µm) and a short domain order of RGO stacked sheets. [14,15,33]

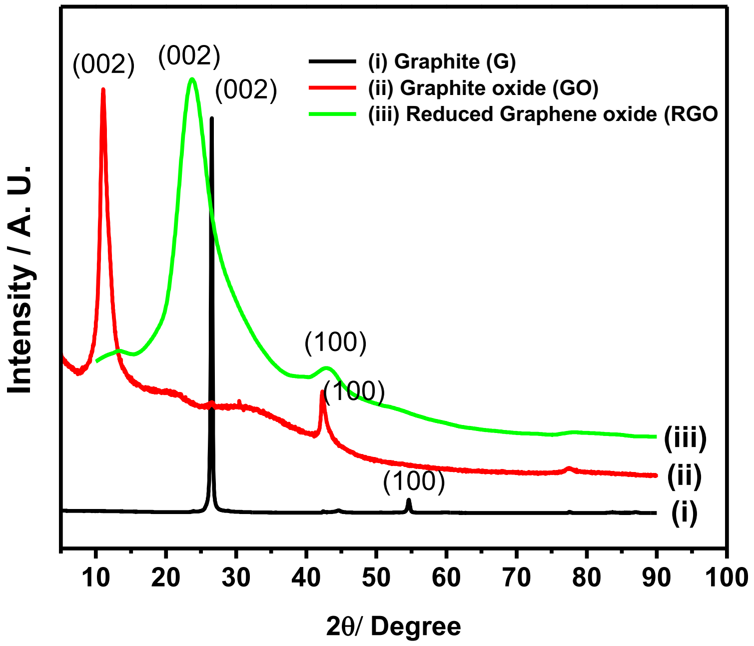

Figure S19. XRD patterns of pristine graphite (i), GO (ii) and RGO (iii).

***SEM/HRTEM analysis:***

SEM images of graphite, GO and RGO samples are shown in Figure S20. Flaky morphology is observed for graphite (Figure S20 (a)) and GO (Figure S20 (b)). In Figure S20, image (c) is the ESEM image of RGO showing exfoliated graphene sheets obtained at 450 °C, whereas images (d), (e) and (f) are the HRTEM images and, there, the SAED pattern clearly indicates the exfoliation of GO by thermal treatment. Exfoliated samples of RGO exhibit a multilayered structure. When compared with graphite and GO, the as-formed RGO after thermal exfoliation reveals turbostatic arrangement of separated graphene sheets, as seen in Figure S20 (c). [14,15,33]

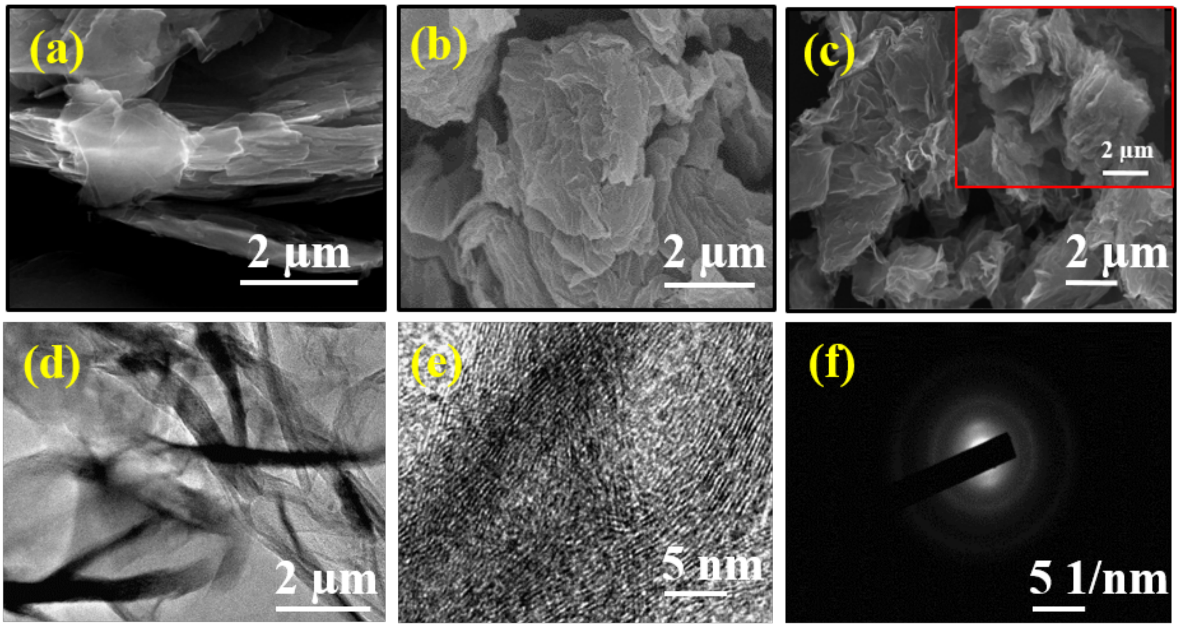

Figure S20. SEM images of samples (a) graphite, (b) GO, (c) RGO and (d)-(f) HRTEM images and SAED patterns of RGO.

***Experimental details related to the electrochemical measurements:***

These peak current values are measured by extrapolation of the baselines of anodic and cathodic peaks as shown in Figure S21.

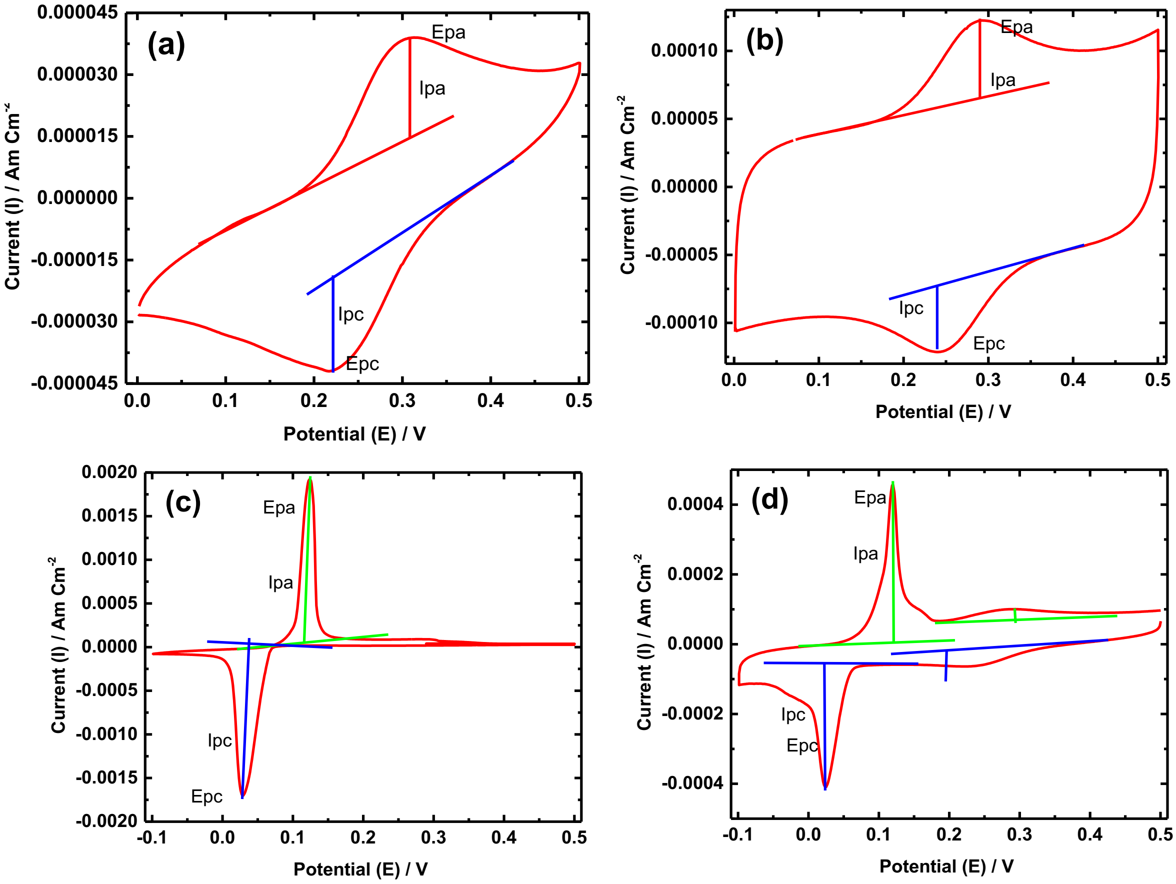

Figure S21. Peak current values measured by extrapolation of the baselines of the anodic and the cathodic peaks for (a) bare GCE, (b) RGO/GCE, (c) Hg/GCE and solid HgNPs/GCE working electrodes in 2 mM $K_4[Fe(CN)_6]/K_3[Fe(CN)_6]$ mixed with 8 ml of 1M KCl aqueous solutions.

### Hydrogen evolution reaction (HER) LSV Plots:

The onset potentials were measured at the point where the current density reaches 1 mA cm$^{-2}$ (Figure S22).

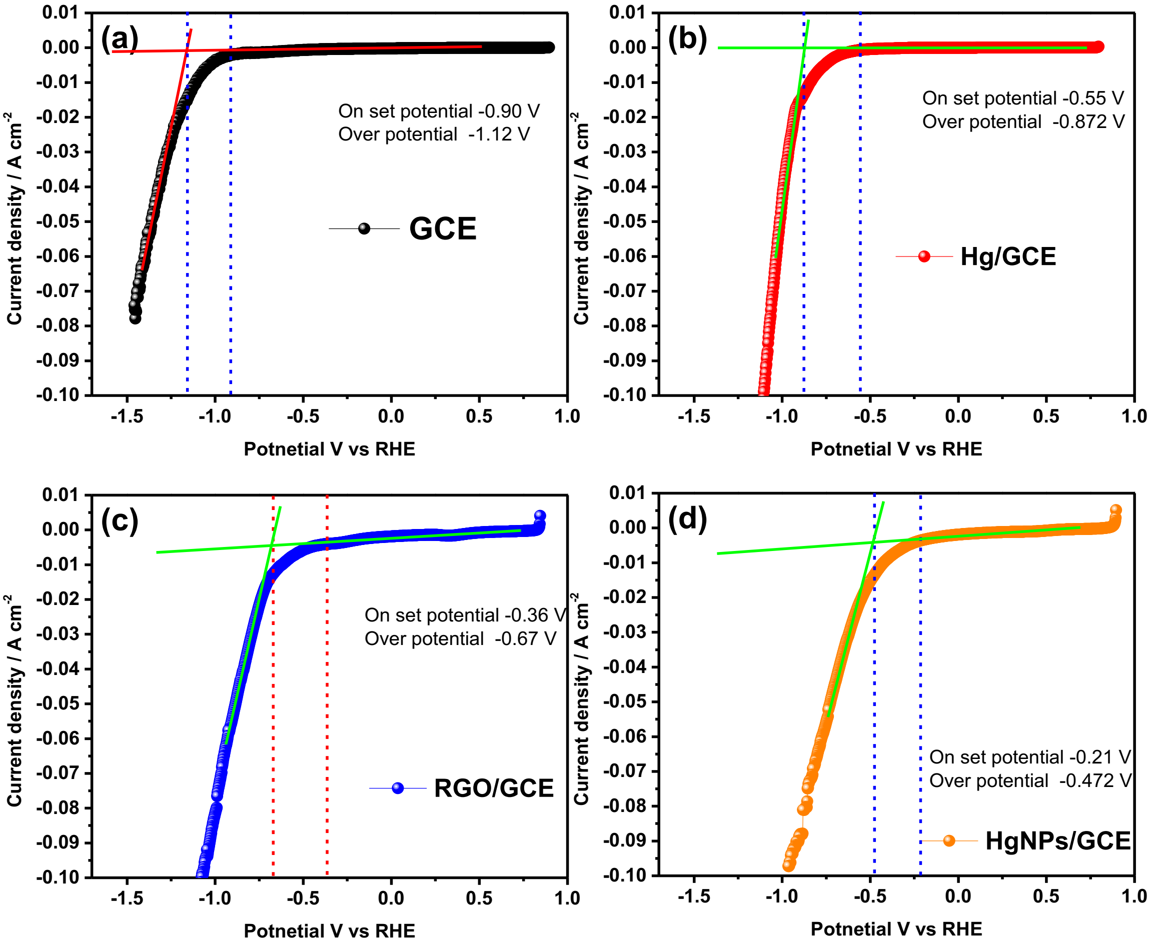

Figure S22. The onset potential and representative over potential values for HER analyses by linear sweep voltammetry with GC, Hg/GC, RGO/GC and HgNPs/GC electrodes, in 0.5 M $H_2SO_4$ solution, at 10mV s$^{-1}$ vs RHE, graphite rods served as counter electrodes.

## Reference:

1 V. B. Kumar, A. Gedanken, G. Kimmel and Z. Porat, *Ultrason. Sonochem.*, 2014, **21**, 1166–1173.

2 R. R. Read and C. Lucarini, *Ind. Eng. Chem.*, 1925, **17**, 480.

3 S. H. Babcock, H. P. Lankelma and E. Vopicka, in *Inorganic Syntheses*, Wiley Blackwell, 2007, vol. 1, pp. 10–11.

4 E. J. Duwell and N. C. Baenziger, *Acta Crystallogr.*, 1955, **8**, 705–710.

5 M. Takaoka, T. Yamamoto, N. Takeda, K. Oshita, T. Tanaka and T. Uruga, in *AIP Conference Proceedings*, 2007, 882, 283–285.

6 F. E. Huggins, G. P. Huffman and G. E. Dunham, *Energy and Fuels*, 1999, **13**, 114–121.

7 F. E. Huggins, N. Yap, G. P. Huffman and C. L. Senior, *Fuel Process. Technol.*, 2003, **82**, 167–196.

8 K. Jiang, S. Siahrostami, T. Zheng, Y. Hu, S. Hwang, E. Stavitski, Y. Peng, J. Dynes, M. Gangisetty, D. Su, K. Attenkofer and H. Wang, *Energy Environ. Sci.*, 2018, **11**, 893–903.

9 L. Zhang, Y. Jia, G. Gao, X. Yan, N. Chen, J. Chen, M. T. Soo, B. Wood, D. Yang, A. Du and X. Yao, *Chem*, 2018, **4**, 285–297.

10 W. Tang, E. Sanville and G. Henkelman, *J. Phys. Condens. Matter*, 2009, **21**, 084204.

11 N. Perkas, G. Amirian, G. Applerot, E. Efendiev, Y. Kaganovskii, A. V. Ghule, B. J. Chen, Y. C. Ling and A. Gedanken, *Nanotechnology*, 2008, **19**, 435604.

12 I. Perelshtein, Y. Ruderman, N. Perkas, J. Beddow, G. Singh, M. Vinatoru, E. Joyce, T. J. Mason, M. Blanes, K. Mollá and A. Gedanken, *Cellulose*, 2013, **20**, 1215–1221.

13 W. S. Hummers and R. E. Offeman, *J. Am. Chem. Soc.*, 1958, **80**, 1339.

14 S. Kumar, C. Selvaraj, L. G. Scanlon and N. Munichandraiah, *Phys. Chem. Chem. Phys.*, 2014, **16**, 22830–22840.

15 L. Zou, F. Kang, Y. P. Zheng and W. Shen, *Electrochim. Acta*, 2009, **54**, 3930–3934.

16 W. Zhang, C. P. Chuu, J. K. Huang, C. H. Chen, M. L. Tsai, Y. H. Chang, C. Te Liang, Y. Z. Chen, Y. L. Chueh, J. H. He, M. Y. Chou and L. J. Li, *Sci. Rep.*, 2015, **4**, 1–8.

17 S. Park, J. An, J. R. Potts, A. Velamakanni, S. Murali and R. S. Ruoff, *Carbon N. Y.*, 2011, **49**, 3019–3023.

18 J. O. M. Bockris, R. Parsons and H. Rosenberg, *Trans. Faraday Soc.*, 1951, **47**, 766–772.

19 H. Ogihara, M. Fujii and T. Saji, *RSC Adv.*, 2014, **4**, 58660–58663.

20 A. Eftekhari, *Int. J. Hydrogen Energy*, 2017, 42, 11053–11077.

21 Jafarian M, Behazin M, Danaee I and Gobal F, *Res. J. Chem. Sci., 2013, 3, 56-63.*

22 A. Frumkin, *Faraday Discuss.*, 1947, **1**, 57–67.

23 P. Luo, L. Jiang, W. Zhang and X. Guan, *Chem. Phys. Lett.*, 2015, **641**, 29–32.

24 W. Zhou, T. Xiong, C. Shi, J. Zhou, K. Zhou, N. Zhu, L. Li, Z. Tang and S. Chen, *Angew. Chemie Int. Ed.*, 2016, **55**, 8416–8420.

25 S. Ghasemi, S. R. Hosseini, S. Nabipour and P. Asen, *Int. J. Hydrogen Energy*, 2015, **40**, 16184–16191.

26 F. Chekin, *Bull. Mater. Sci.*, 2015, 38, 887–893.

27 Y. Li, L. A. Zhang, Y. Qin, F. Chu, Y. Kong, Y. Tao, Y. Li, Y. Bu, D. Ding and M. Liu, *ACS Catal.*, 2018, **8**, 5714–5720.

28 X. Chen, J. Zheng, X. Zhong, Y. Jin, G. Zhuang, X. Li, S. Deng and J. G. Wang, *Catal. Sci. Technol.*, 2017, **7**, 4964–4970.

29 D. Hou, W. Zhou, K. Zhou, Y. Zhou, J. Zhong, L. Yang, J. Lu, G. Li and S. Chen, *J. Mater. Chem. A*, 2015, **3**, 15962–15968.

30 Y. Yang, J. Liu, S. Guo, Y. Liu and Z. Kang, *J. Mater. Chem. A*, 2015, **3**, 18598–18604.

31 Z. Xing, D. Wang, Q. Li, A. M. Asiri and X. Sun, *Electrochim. Acta*, 2016, **210**, 729–733.

32 J. Wang, H. Zhu, J. D. Chen, B. Zhang, M. Zhang, L. N. Wang and M. L. Du, *Int. J. Hydrogen Energy*, 2016, **41**, 18044–18049.

33 I. K. Moon, J. Lee, R. S. Ruoff and H. Lee, *Nat. Commun.*, 2010, **1**, 1–6.

34 C. Zhang, W. Lv, X. Xie, D. Tang, C. Liu and Q. H. Yang, *Carbon N. Y.*, 2013, 62, 11–24.